Writing and detecting topological charges in exfoliated Fe_{5-x}GeTe₂

Alex $Moon^{\S, \pounds}$, Yue Li^{Ξ} , Conor McKeever $^{\$}$, Brian W. Casas § , Moises Bravo § , Wenkai Zheng $^{\S, \pounds}$, Juan Macy $^{\S, \pounds}$, Amanda K. Petford-Long $^{\Xi, \Xi}$, Gregory T. McCandless § , Julia Y. Chan § , Charudatta Phatak $^{\Xi, \Xi}$, Elton J. G. Santos $^{\$, \pm, *}$, and Luis Balicas $^{\S, \pounds, *}$

§National High Magnetic Field Laboratory, 1800 E. Paul Dirac Dr. Tallahassee, FL 32310, USA.

[£]Department of Physics, Florida State University, 77 Chieftan Way, Tallahassee, FL 32306, USA.

*Institute for Condensed Matter and Complex Systems, School of Physics and Astronomy, The

University of Edinburgh, EH9 3FD, UK.

¹Department of Chemistry and Biochemistry, Baylor University, Waco, TX 76798, USA.

²Department of Materials Science and Engineering, Northwestern University, Evanston, 60208, IL, USA.

[†]Higgs Centre for Theoretical Physics, The University of Edinburgh, EH9 3FD, UK.

ABSTRACT: Fe_{5-x}GeTe₂ is a promising two-dimensional (2D) van der Waals (vdW) magnet for practical applications, given its magnetic properties. These include Curie temperatures above room temperature, and topological spin textures – TST (both merons and skyrmions), responsible for a pronounced anomalous Hall effect (AHE) and its topological counterpart (THE), which can be

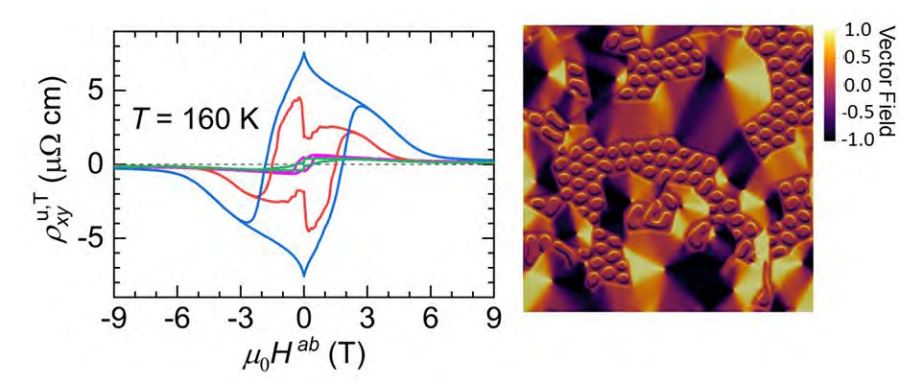
harvested for spintronics.

Here, we show that both the

AHE and THE can be

amplified considerably by

just adjusting the thickness



of exfoliated Fe_{5-x}GeTe₂, with THE becoming observable even in zero magnetic field due to a field-induced unbalance in topological charges. Using a complementary suite of techniques, including electronic transport, Lorentz transmission electron microscopy, and micromagnetic simulations, we reveal the emergence of substantial coercive fields upon exfoliation, which are absent in the bulk, implying thickness-dependent magnetic interactions that affect the TST. We detected a 'magic' thickness $t \sim 30$ nm where the formation of TST is maximized, inducing large magnitudes for the topological charge density ($\sim 6.45 \times 10^{20} \text{ cm}^{-2}$), and the concomitant anomalous ($\rho_{xy}^{A,\text{max}} \cong 22.6 \,\mu\Omega$ cm) and topological ($\rho_{xy}^{u,T} \cong 15 \,\mu\Omega$ cm) Hall resistivities at $T \sim 120$ K. These values for $\rho_{xy}^{A,\text{max}}$ and $\rho_{xy}^{u,T}$ are higher than those found in magnetic topological insulators and, so far, the largest reported for 2D magnets. The hitherto unobserved THE under zero magnetic field could provide a platform for the writing and electrical detection of TST aiming at energy-efficient devices based on vdW ferromagnets.

KEYWORDS: merons, skyrmions, topological charges, anomalous Hall-effect, topological Hall-effect.

The study of magnetism in the two-dimensional (2D) limit has been pivotal for the development of critical phenomena and strongly correlated phases in ultrathin compounds¹⁻³. Such van der Waals (vdW) magnetism has seen a recent resurgence due to the advent of layered magnetic compounds displaying a magnetic ground state even when exfoliated down to the monolaver limit⁴⁻ ⁷. Since 2D magnetism is not ruled out by the non-existence of crystalline magnetic anisotropy, as recently demonstrated⁸, several materials have been explored towards for fundamental interest and practical applications, in particular semiconducting tri-halides⁹. Among known vdW layered magnets, the metallic ferromagnets belonging to the Fe_{n-x}GeTe₂ family, and its doped variants, display the highest known Curie temperature (T_c) with $T_c \sim (205 \text{ K} - 230 \text{ K})^8$ for n = 3, $\sim 278 \text{ K}^{10}$ for n = 4, $(\sim 270 \text{ K} - 330 \text{ K})^{11}$ for n = 5, and $> 400 \text{ K}^{12}$ for Ni-doped Fe₅GeTe₂. In these compounds, not only is magnetism observed in very thin layers, but there is also tunability via a perpendicular electric field. In tri-layered Fe_{3-x}GeTe₂, T_c increases from ~ 100 K up to room temperature via the use of ionic liquid gating¹³. Meanwhile, the ground state of two unit cell thick Fe_{5-x}GeTe₂¹⁴ and bulk Fe_{3-x}GeTe₂¹⁵ switches from ferromagnetic to antiferromagnetic upon solid proton electrolyte gating. Despite being centrosymmetric, implying a priori the absence of the Dzyaloshinskii– Moriya interaction¹⁶ (DMI), these compounds are prone to display topological spin textures, such as skyrmions¹⁷⁻¹⁹, merons¹⁹⁻²¹, and complex domain boundaries between stripe domains²².

Topological spin textures such as skyrmions, are vortex-like nanometric spin textures that carry an integer topological number, or topological charge, describing how many times the magnetic moments composing it wrap around a sphere. In contrast, merons are characterized by a half integer topological charge. Such textures are characterized by a finite value of the scalar field spin chirality, $\chi_{ijk} = \overrightarrow{S_i} \cdot (\overrightarrow{S_j} \times \overrightarrow{S_k})$, which is a fictitious magnetic field that bends the electronic orbits, generating the so-called topological Hall effect (THE)²³⁻²⁶. In magnetic compounds, the

THE is usually treated as an additive contribution to the conventional and anomalous Hall responses:

$$\rho_{xy} = \rho_{xy}^{\text{N}} + \rho_{xy}^{\text{A}} + \rho_{xy}^{\text{T}} \tag{1}$$

where $\rho_{xy}^{N} = R_0 B$ is the conventional Hall response, with R_0 being the Hall coefficient, $\rho_{xy}^{A} = S_H M \rho_{xx}^n$ the anomalous Hall effect (AHE) term, with S_H being the anomalous Hall constant, B the induction field, M the magnetization, ρ_{xx}^{n} a power of the magnetoresistivity, and ρ_{xy}^{T} the THE contribution. Through a semiclassical theoretical approach that includes the solution of the Boltzmann equation, it was recently shown that these contributions are indeed additive, with the intrinsic anomalous Hall effect resulting from the Berry curvature (acquired by charge carriers as they move) in momentum-space, and the topological term from the Berry curvature in real-space²⁷. Based on a scaling analysis proposed by Ref. ²⁸, it was recently argued that the anomalous Hall effect observed in Fe_{5-x}GeTe₂ is dominated by the intrinsic contribution²⁹. This implies that ρ_{xy}^{A} should be dominated by either the Berry phase resulting from carriers scattering from the topological spin textures, or the Karplus Luttinger term³⁰, instead of extrinsic mechanisms such as skew scattering or side jumps³¹.

Given that spin chirality is a scalar and not a vector field, it can deflect moving charges regardless of the orientation of an applied external magnetic field. This point is illustrated by the observation of an antisymmetric Hall-like signal in both Fe_{3-x}GeTe₂ (Ref.³²) and Fe_{5-x}GeTe₂ (Ref.¹⁹) when the external magnetic field is oriented along the electrical currents, or in the absence of Lorentz force. In both systems, this unconventional THE-like signal is found to be magnetic-field dependent, given that the field alters the spin textures (and associated spin chirality) responsible for this unconventional THE or $\rho_{xy}^{u,T}$. In the case of Fe_{3-x}GeTe₂, $\rho_{xy}^{u,T}$ peaks at low temperatures in the vicinity of $\mu_0 H \cong 4.5$ T, with this behavior being mimicked by both the

unconventional topological Nernst response, $S_{xy}^{u,T}$, and the topological thermal Hall response, $\kappa_{xy}^{u,T}$, measured with the thermal gradient ∇T aligned along $\mu_0 H$ in the ab-plane³². Here, the term "unconventional" refers to the unconventional measurement configurations.

An intriguing aspect of Fe_{5-x}GeTe₂, and its doped variants, is the fact that its magnetic domains, and associated spin textures, can be modified via simple exfoliation^{21, 29, 33, 34}. Ref. ²¹ attributes such magnetic transformations to thickness-dependent changes in the relative strengths of the exchange constants, magnetic uniaxial anisotropy, and magnetic dipole interaction. This leads to thickness-dependent magnetic phase diagrams²¹, and, apparently, also to the observation of skyrmions in $(Fe_{0.5}Co_{0.5})_{5-x}GeTe_2$ in a narrow range of thicknesses³⁴, i.e., from $\sim 0.1 \mu m$ to ~ 1 um. Seemingly, exfoliation increases the relevance of the dipolar interactions in detriment of the DMI, increasing also the magnetic fluctuations that lead to lower Curie temperatures, effectively making the interplanar exchange coupling less relevant to 2D magnets. This modulates the spin texture, for instance, in (Fe_{0.5}Co_{0.5})_{5-x}GeTe₂, the Néel skyrmion size d was reported to behave as d $\propto t^{1/2}$, with t being the thickness, hence following Kittel's law³⁴. It also leads to the emergence of hysteresis in both the magnetoresistivity and AHE in exfoliated samples²⁹ although this is absent in bulk crystals (see, Fig. S1). In thin lamellas of Fe_{1.9}Ni_{0.9}Pd_{0.2}P, square shaped antiskyrmions are observed to transition to elliptical like skyrmions as the lamella thickness t is reduced to $t \sim 50$ nm and claimed to result from the increased relevance of the dipolar interaction, relative to the DMI, at t is reduced³⁵. It is, therefore, pertinent to ask if, and how, the spin textures evolve as a function of layer thickness and if such evolution might affect the unconventional THE^{20, 36} observed in Fe₅₋ *x*GeTe₂.

Here, we evaluate the unconventional THE $(\rho_{xy}^{u,T})$ and AHE (ρ_{xy}^{A}) responses of Fe_{5-x}GeTe₂ as a function of both the crystal thickness t within 12 nm $\leq t \leq$ 65 nm and temperature. For fields

parallel to electrical currents flowing along a planar direction, we find a coercive field $\mu_0 H_c^{ab} > 10$ $\mu_0 H_c^c$, where $\mu_0 H_c^{ab}$ and $\mu_0 H_c^c$ are the coercive fields seen in the THE and AHE responses for $\mu_0 H$ parallel to the ab-plane and the c-axis, respectively. This implies a rotation of the magnetic hard axis of Fe_{5-x}GeTe₂ upon exfoliation, from the c-axis towards the ab-plane, in contrast to what is observed for bulk samples. Experimentally, we find that this reorientation leads to a very large enhancement of both ρ_{xy}^{A} and $\rho_{xy}^{u,T}$, with both quantities peaking at a thickness $t \cong 30$ nm. Our micromagnetic simulations indicate that there is a maximum in the topological charge density around this thickness, located between the complete spin homogeneity of very thin films due to an exchange-dominated regime, and the spin inhomogeneity intrinsic to thick films, dominated by the dipolar interactions. We also observe the emergence of a very pronounced hysteresis in the THE, particularly in a temperature range where hysteresis remains completely absent in the longitudinal magnetoresistivity. This implies that the hysteresis observed at higher temperatures is not dominated by the movement and pinning of ferromagnetic domain walls. Instead, we argued that remnant chiral spin textures provide a Hall-like signal even after the external magnetic field is suppressed. This is supported by both our Lorentz transmission electron microscopy (LTEM) measurements that reveal remnant skyrmions upon magnetic field removal, and our micromagnetic simulations indicating that the maximum meron density, and, hence, topological charge-density, peaks at $\mu_0 H = 0$ T. The ensemble of our observations is consistent with intrinsic anomalous and topological Hall responses modulated by the evolution of the spin textures as a function of thickness, temperature, and magnetic field. They also point to the possibility of writing remnant topological spin textures with a magnetic field and electrically detecting them via a topological Hall voltage. This exposes the potential of Fe_{5-x}GeTe₂ for the development of magnetic memory elements and spintronics in general.

RESULTS/DISCUSSION

Intrinsic versus extrinsic contributions to the anomalous Hall effect in Fe_{5-x}GeTe₂

Figure 1 displays the electrical resistivity, ρ_{xx} , as a function of the temperature, T, for an exfoliated Fe_{5-x}GeTe₂ flake of thickness t = 35 nm that was transferred onto pre-patterned Ti:Au electrical contacts and subsequently encapsulated with an exfoliated h-BN crystal. ρ_{xx} displays a T-dependence and values akin to those seen in bulk samples¹¹ implying that the exfoliated material is not degraded by the fabrication process, which is performed under inert conditions. A sharp decrease in ρ_{xx} is observed upon cooling below the magneto-structural transition at $T_s \sim 110 \text{ K}^{11}$. Upon application of a magnetic field (Fig. 1b), $\rho_{xx}(\mu_0 H^c)$ is observed to decrease (negative magnetoresistivity) implying the suppression of spin-scattering processes.

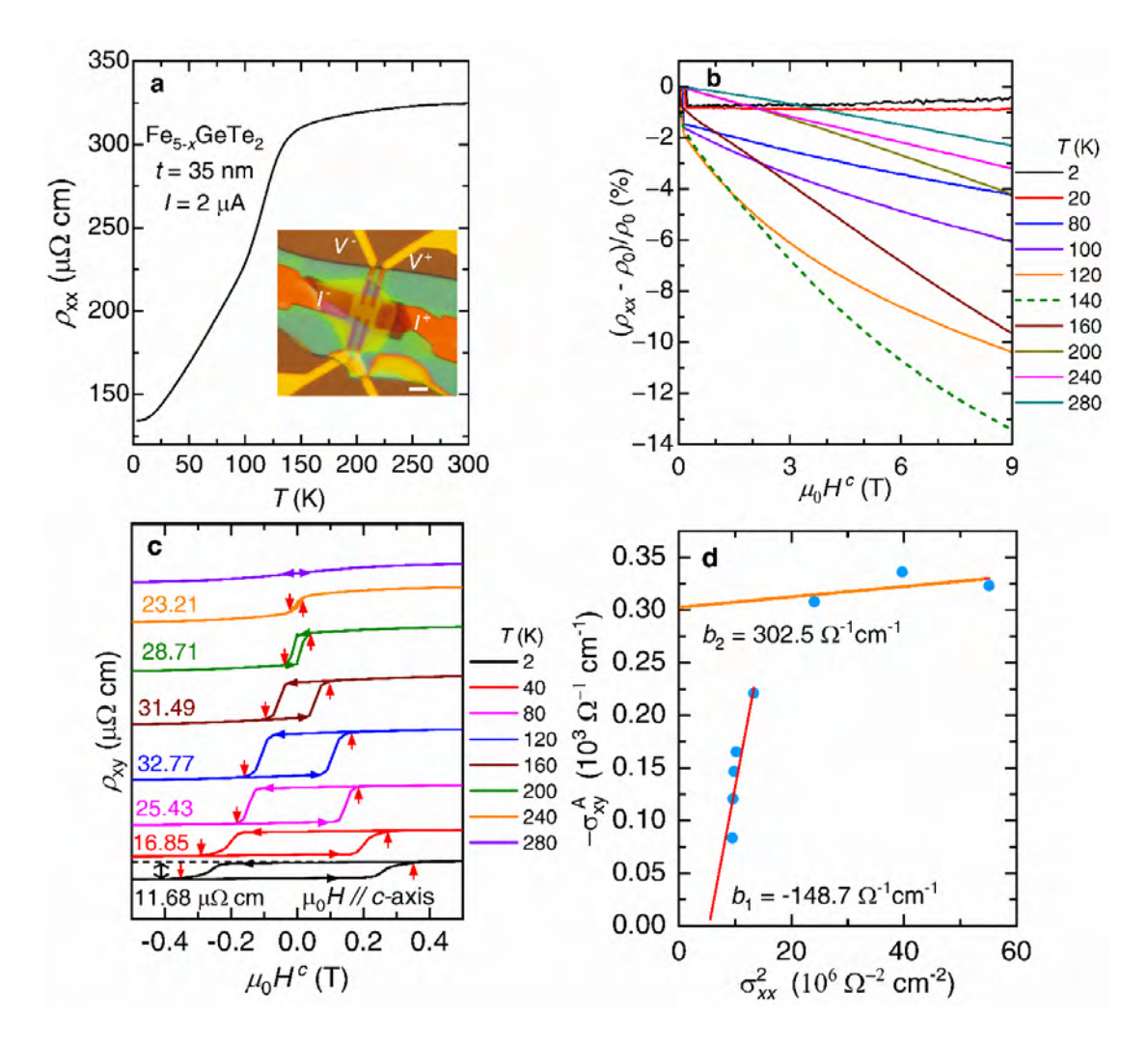


Figure 1. Hysteresis and intrinsic contribution to the anomalous Hall effect in exfoliated Fe_{5-x}GeTe₂. (a) Resistivity (ρ_{xx}) as a function of T (K) for a flake of thickness t = 35 nm transferred onto pre-patterned Ti:Au contacts and subsequently encapsulated with a top h-BN layer. Inset: Micrograph of the sample, where the scale bar (horizontal white line) indicates a lateral dimension of 5 μ m. (b) Magnetoresistivity (($\rho_{xx} - \rho_0$)/ ρ_0) as a function of the magnetic field $\mu_0 H^c$ applied along the c-axis for several temperatures for the heterostructure in a. The maximum of the magnetoresistivity is reached at 140 K, as indicated by the dashed green line. (c) Raw Hall resistivity (ρ_{xy}) as a function of $\mu_0 H^c$ for several values of T. We notice the presence of an AHE response as well as the emergence of a large irreversibility/hysteresis in the Hall response, which is absent in bulk single crystals. Red vertical arrows indicate the values of the coercive field $\mu_0 H_c^c$. (d) Anomalous Hall conductivity (σ_{xy}^2) as a function of the square of the conductivity (σ_{xx}^2). Two regimes were observed resulting in the linear

fits b_1 (red) and b_2 (orange), above and below, respectively, the magneto-structural transition at T_s . These coefficients provide the intrinsic contribution to the anomalous Hall response.

The sharp step seen at low fields results from the emergence of hysteresis, confirming the hard ferromagnetic response^{29, 37} of exfoliated Fe_{5-x}GeTe₂. The most pronounced negative magnetoresistivity is observed around T = 120 K to 140 K, or just above T_s , implying that pronounced spin fluctuations precede the transition at T_s . At the lowest T_s and beyond the coercive field $\mu_0 H_c^c$, the magnetoresistivity becomes slightly positive, implying the near total suppression of thermally activated spin fluctuations. The hysteresis and associated coercive field $\mu_0 H_c^c$ (indicated by the vertical red arrows (Fig. 1c)) is more clearly exposed by measurements of the AHE resistivity $\rho_{xy}^{A}(\mu_0 H^c)$. The hysteresis in the AHE response is reflected by $\rho_{xx}(\mu_0 H^c)$ (Supplementary Figure S1). Note, that in Fig. 1c for fields oriented along the c-axis the coercive field for t = 35 nm (~12 unit cells or 36 layers) approaches $\mu_0 H_c^c \sim 0.4$ T at T = 2 K, with this value being considerably larger than those reported in Ref. ²⁹ for samples having thicknesses ranging from 4 to 15 layers. This suggests that the maximum values of $\mu_0 H_c^c$ are observed in samples having thicknesses ranging between 10- and 20-unit cells and implies thickness-dependent domains, spin textures³⁴, and magnetic axial anisotropy affecting the ferromagnetic hardness of $Fe_{5-x}GeTe_2$.

Given that both extrinsic and intrinsic mechanisms contribute to the AHE of a ferromagnet, before discussing the thickness dependence of ρ_{xy}^{A} in Fe_{5-x}GeTe₂, one should expose the dominant mechanism. According to the scaling analysis of Ref.²⁸, the anomalous Hall conductivity follows the empiric relation:

$$\sigma_{xy}^{A} = -\frac{\rho_{xy}^{A}}{(\rho_{xy}^{A})^{2} + \rho_{xx}^{2}} = -(\alpha \sigma_{xx0}^{-1} + \beta \sigma_{xx0}^{-2})\sigma_{xx}^{2} - b$$
 (1)

where, $\sigma_{xx0}=1/\rho_{xx0}$ is the residual conductivity, $\sigma_{xx}=\rho_{xx}/(\rho_{xx}^2+\rho_{xy}^2)$ is the conductivity, α and β are the skew scattering and side-jump scattering terms, respectively, and b is the intrinsic term due to either the Karplus-Luttinger mechanism³⁰ or the scalar spin chirality. Therefore, as the temperature is varied, σ_{xy}^{A} should scale linearly with $-\sigma_{xx}^{2}$, with the intercept providing the magnitude of the intrinsic term b. A plot of σ_{xy}^{A} as a function of σ_{xx}^{2} (Fig. 1d) reveals two distinct regimes that are linear in $-\sigma_{xx}^2$. These are indicated by linear fits both above (red line) and below (orange line) $T_s \sim 110$ K that yield very distinct slopes as well as intercepts, or b values. Below T_s , one extracts $b_2 \cong 303 \ (\Omega \ cm)^{-1}$ which is a factor of ~ 3 smaller than the value extracted by us for Fe₃GeTe₂, i.e., $b \sim 940 \ (\Omega \ \text{cm})^{-1}$. This last value is close to $b \sim 1100 \ (\Omega \ \text{cm})^{-1}$ obtained at room T for Fe films epitaxially grown on undoped GaAs $(001)^{28}$. For this temperature regime, $T < T_s$, the slope $s_2 = (\alpha_2 \sigma_{xx0}^{-1} + \beta_2 \sigma_{xx0}^{-2})$ yields a value of 5 x 10⁻⁷ (Ω cm)⁻¹ $\ll b_2$ indicating that σ_{xy}^{A} is dominated by the intrinsic mechanism. In contrast, for $T > T_s$ the intercept decreases by a factor of ~2 while also changing its sign, such that $b_1 \sim -150 \; (\Omega \text{cm})^{-1}$. This sign change might indicate an electronic reconstruction at T_s or a change in the relative contributions of the Karpus-Luttinger³⁰ and spin chirality mechanisms. The slope on the other hand, increases by almost two orders of magnitude up to $s_1 \sim 3 \times 10^{-5}$ (Ω cm)⁻¹ $\ll |-150$ (Ω cm)⁻¹|, implying that the intrinsic mechanism still dominates the AHE for $T > T_s$.

It was reported that the spin textures observed in Fe_{5-x}GeTe₂, and related phase diagrams are thickness dependent^{21, 29, 33} due to a thickness-dependent competition between the relevant exchange interaction(s), the dipole–dipole coupling³³, and a possible reorientation of the perpendicular magnetic anisotropy (PMA). Some of these studies^{29, 33} focused on very thin flakes, *i.e.*, from monolayers (1L) to ~15L thick $^{13, 38-40}$.

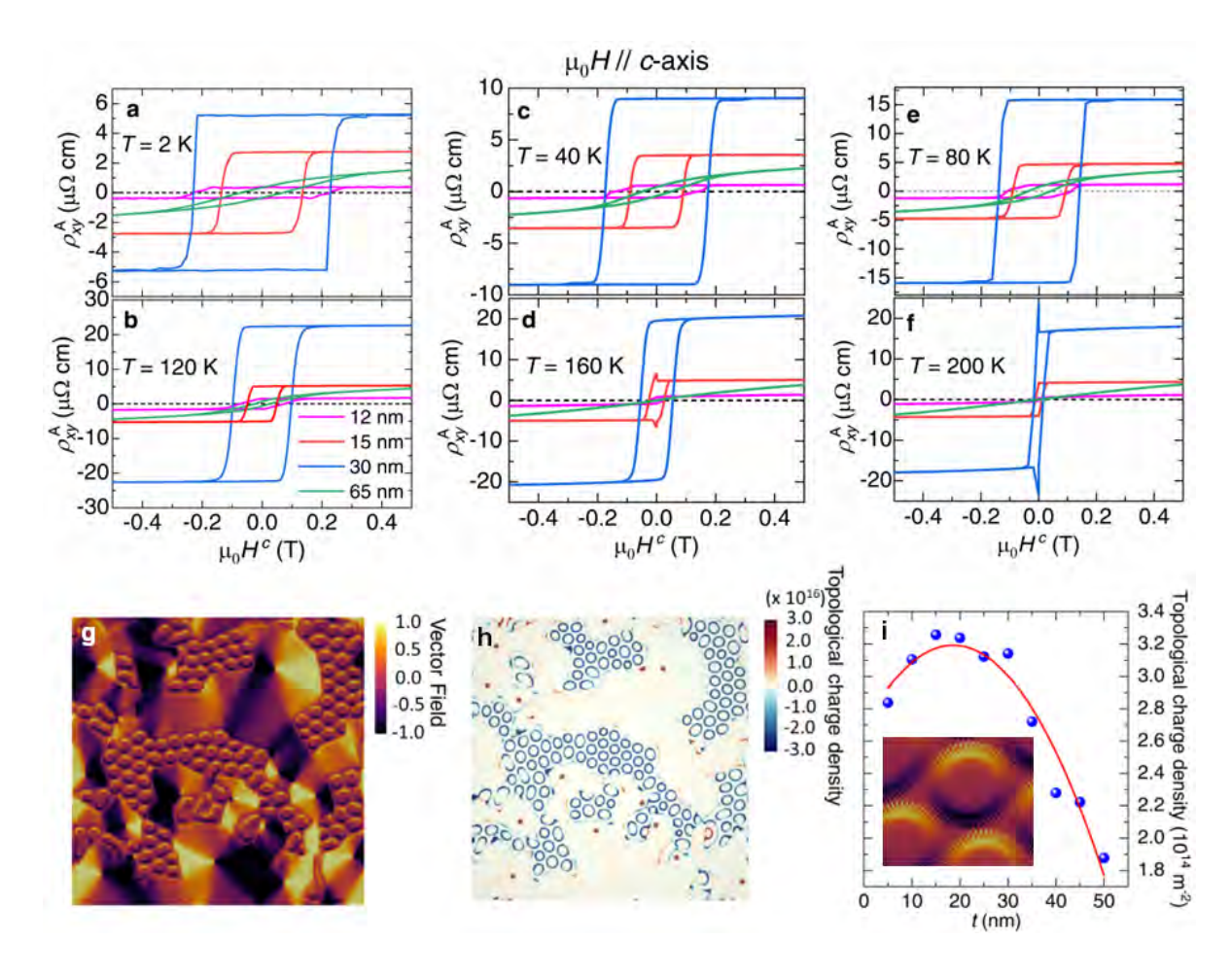


Figure 2. Anomalous Hall response ρ_{xy}^A and micromagnetic simulations. (a-f) ρ_{xy}^A as function of $\mu_0 H$ applied along the c-axis for six temperatures, 2, 40, 80, 120, 160 and 200 K, respectively. Magenta, red, blue, and green traces correspond to crystal thicknesses of 12, 15, 30 and 65 nm, respectively. Note the increased loop squareness with the increase of the coercive field $\mu_0 H_c^c$ as T is lowered, and the increase in the AHE response as the number of layers, n, decreases. The maximum values occurred for an Fes-xGeTe2 crystal of 30 nm thickness. (g) Snapshot of the magnetization domains obtained via micromagnetic simulations at zero field and 0 K, including domains with their magnetization oriented within the conducting planes and domains with the magnetization oriented perpendicular to the planes. As discussed in Refs. 20, 21,36, several domain walls meet at a planar spin vortex that contains a meron at its center. The application of a transverse magnetic field stabilizes skyrmions in domains characterized by an out-of-plane magnetization component 35. (h) Calculated topological charge density associated with domain structure shown in g. (i) Topological charge density as a function of sample thickness, showing a maximum for 15 nm $\leq t \leq 25$ nm, nearly in agreement with the t-dependence of

 $\rho_{xy}^{A}(t)$. The slight fluctuation in the values of the topological charge (blue dots) are due to several realizations (~10 times) of the random spin seeds that were subsequently averaged for each thickness. The red line is a simple fit to an order-3 polynomial. Inset: magnified image of a simulated magnetic skyrmion.

Apparently, the Curie temperature T_c remains nearly constant as a function of t, decreasing only for the bilayers and monolayers²⁹. However, the magnetic phase diagram of Fe_{5-x}GeTe₂ measured on much thicker crystals, from 67L to 112L, was still found to be thickness dependent²¹, although one would naively expect multilayered crystals to display essentially bulk behavior. To evaluate the effects of manipulating the magnetic phase diagram of Fe_{5-x}GeTe₂ via exfoliation, we measured the AHE in crystals with thicknesses ranging from 12 nm to 65 nm, or ~12L to ~65L. These crystals are thick enough to remain in the bulk limit, therefore, preserving the previously reported chiral spin textures^{20, 36}, while being thin enough to affect their phase diagram as a function of the temperature, magnetic-field, and thickness²¹.

Thickness dependence of the anomalous Hall response and micromagnetic simulations

For magnetic fields oriented along the c-axis, the anomalous Hall response (Figure 2) is found to display a marked hysteresis, in contrast to what is seen for bulk crystals (Supporting Figure S1), with the coercive field H_c^c increasing as T is lowered, as previously reported in Ref.²⁹. The coercivity $H_c^c \sim 0.2-0.3$ mT is a factor of ~2 smaller than the values reported for Fe_{3-x}GeTe₂ at low temperatures⁴¹. Albeit, one still observes $H_c^c \geq 0.1$ T for $T \geq 160$ K, in contrast to $\mu_0 H_c^c \sim$ zero for Fe_{3-x}GeTe₂ when $T \geq 135$ K⁴¹. A maximum in resistivity, $\rho_{xy}^{A,\text{max}} \cong 22.6$ $\mu\Omega$ cm, is observed for the anomalous Hall response of the 30 nm thick crystal at T = 120 K which is just above the structural transition at $T_s \cong 110$ K. This value is nearly 5x larger than the one displayed by the t = 65 nm sample and over ~3.6 times larger than $\rho_{xy}^{A,\text{max}} \sim 6$ $\mu\Omega$ cm extracted from bulk

crystals³⁶. This enhancement is very difficult to reconcile with extrinsic mechanisms, given that the resistivity, ρ_{xx} , as a function of T, and, hence, the residual resistivity, ρ_{xx0} , of the exfoliated crystals, are identical to those of the bulk crystals (Fig. 1a, and Eq. 1). To put this value in perspective, it is only a factor of 2 smaller than the maximum value of ρ_{xy}^{A} in Co₃Sn₂S₂, a compound claimed to display a giant anomalous Hall response⁴² around the same range of temperatures. We are led to conclude that in Fe_{5-x}GeTe₂, ρ_{xy}^{A} is dominated by the intrinsic contribution associated with chiral spin textures, which are modulated by the thickness of the layers. Our data indicates that the maximum values are observed in crystals with thickness ranging from 20 nm to 40 nm. This conclusion is supported by our micromagnetic simulations (see Methods for details and Fig. 2g) where we mimicked the ferromagnetic domain structure of exfoliated Fe_{5-x}GeTe₂³⁶. Some of these domains are characterized by a random in-plane magnetic anisotropy while others display an out-of-plane anisotropy. Our simulation approach resulted in the successful description of the LTEM contrast in Fe_{5-x}GeTe₂ in which we observed merons at the converging domain boundaries between planar ferromagnetic domains, ³⁶ in addition skyrmions are stabilized under a perpendicular magnetic field, for domains having an out of plane anisotropy. This leads to a pronounced density of topological charges associated with the merons and skyrmions (Fig. 2h). It turns out that the topological charge density inherent to these spin textures is strongly modulated by the sample thickness, displaying the largest density for thicknesses ranging between 15 and 30 nm in decent agreement with our experimental observations (Fig. 2i). Exfoliation favors the dipolar interaction which leads to a higher degree of order among spin textures. It also favors skyrmions of smaller radii. Both effects conspire to increase the topological charge density within this range of thicknesses. Notice that all crystal thicknesses display a maximum in the anomalous and topological Hall responses around T ~ 120 K, suggesting a maximum topological charge density around this temperature, regardless of sample thickness.

The unconventional topological Hall effect

Upon rotating $\mu_0 H$ from the c-axis towards the ab-plane, one observes a sharp increase in the coercive field, $\mu_0 H_c$ (Figs. 3a-3b), by over one order of magnitude, for an Fe_{5-x}GeTe₂ crystal with thickness t=15 nm. This increase i) indicates that the magnetic easy axis in exfoliated crystals is no longer in the ab-plane as is the case for bulk Fe_{5-x}GeTe₂ single-crystals³⁶, and ii) that it surpasses, by a factor >2, the values of $\mu_0 H_c^{ab}$ for Fe_{3-x}GeTe₂ whose magnetic hard axis remains within the ab-plane in exfoliated crystals⁴¹. Notice that the large values of $\mu_0 H_c^{ab}$ in exfoliated Fe_{5-x}GeTe₂, relative to those of exfoliated Fe_{3-x}GeTe₂ crystals, cannot be attributed to a higher degree of disorder that would pin magnetic domain walls.

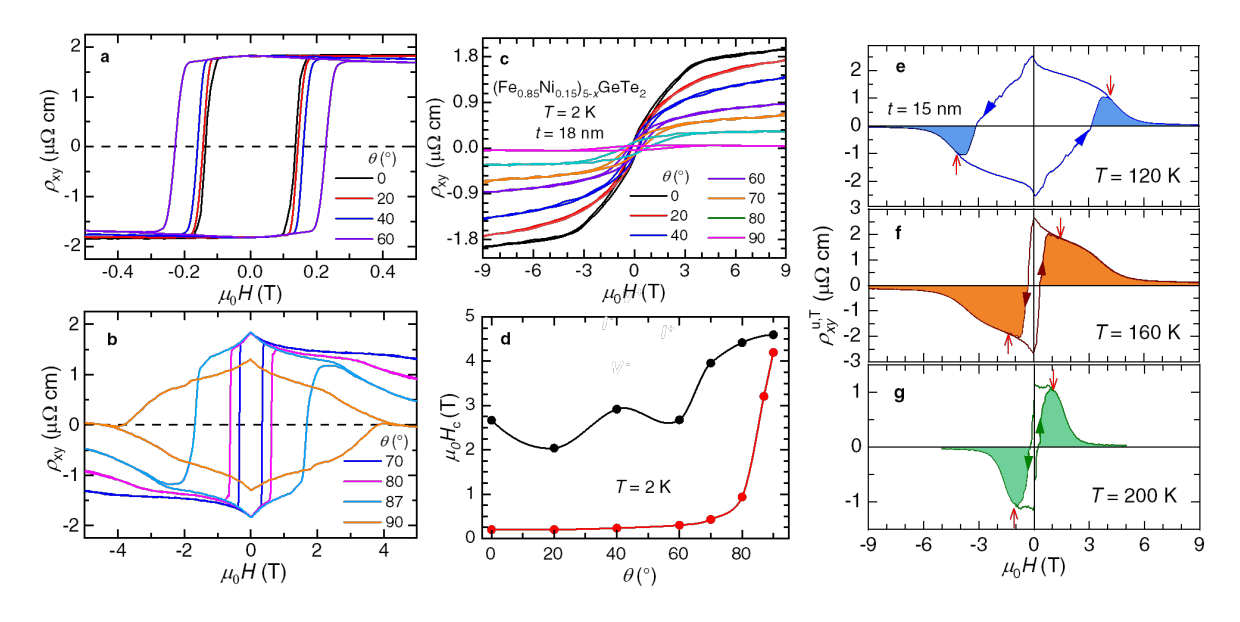


Figure 3. Coercivity as a function of magnetic field orientation and unconventional THE. (a-b) Raw Hall resistivity ρ_{xy} at T=2 K as a function of the angle θ between μ_0H and the c-axis of a t=15 nm thick Fe_{5-x}GeTe₂ crystal. We observed an increase by more than one order of magnitude in the coercive field H_c as μ_0H is rotated towards the ab-plane. (c) Raw ρ_{xy} measured from a Ni-doped Fe_{5-x}GeTe₂ crystal (composition (Fe_{0.85}Ni_{0.15})s-xGeTe₂) of thickness t=18 nm. Note the similar values of the saturating anomalous Hall response with respect to the value for the t=15 nm thick Fe_{5-x}GeTe₂ crystal. In contrast, (Fe_{0.85}Ni_{0.15})s-xGeTe₂ displays one order of magnitude larger values for $\mu_0H_c^c$, probably due to the disorder inherent to its alloy character. (d) Coercive

fields, $\mu_0 H_c$, as a function of the angle θ between $\mu_0 H$ and the interlayer c-axis for both (Fe_{0.85}Ni_{0.15})_{5-x}GeTe₂ (t = 18 nm, black markers) and Fe_{5-x}GeTe₂ (t = 15 nm, red markers) at T = 2 K. For both compounds, H_c increases rapidly as θ surpasses 70°, but for both samples it displays similar values around θ = 90°. (e), (f) and (g) Unconventional THE response $\rho_{xy}^{u,T}$ resulting from an unconventional measurement geometry, namely magnetic field parallel to the electrical current using a Hall geometry for the voltage leads, and for three temperatures T = 120 K, 160 K, and 200 K, respectively. We note extremely large coercive fields $\mu_0 H_c^{ab}$ (indicated by red arrows) that are over one order of magnitude larger than $\mu_0 H_c^c$ at the same temperatures, and the broad peak in $\rho_{xy}^{u,T}$ for fields beyond $\mu_0 H_c^{ab}$.

This point is illustrated by the Hall resistivity of an exfoliated Ni-doped Fe_{5-x}GeTe₂ singlecrystal (t = 18 nm, Fig. 3c), with composition (Fe_{0.85}Ni_{0.15})_{5-x}GeTe₂. Details concerning single crystal X-ray diffraction are provided by Table 1 in Methods, Supporting Table S1, and Supporting Figure S3, indicating a homogeneous solid solution whose crystallographic structure can be well refined. Ni doping was found to increase the Curie temperature of Fe_{5-x}GeTe₂ although the exact mechanism is not understood¹². The authors of Ref. ¹² mention a few possible mechanisms such as site occupancy, structural modifications that alter the relevant exchange couplings, and the electron doping. For $(Fe_{0.85}Ni_{0.15})_{5-x}GeTe_2$, and for μ_0H parallel to the c-axis, one observes a marked increase in the magnetic field required to saturate $\rho_{xy}^{A}(\mu_0 H, \theta)$. Therefore, Ni doping also increases $\mu_0 H_c^c(\mu_0 H, \theta)$, to a value that now exceeds the corresponding ones for Fe_{5-x}GeTe₂ by one order of magnitude, due to structural disorder. However, for fields close to the ab-plane, the Ni-doped crystal displays almost the same values of $\mu_0 H_c^{ab}(\theta = 90^\circ)$ as the undoped compound. This implies that structural disorder, expected to pin the movement of magnetic domain walls upon sweeping a magnetic field, has little influence on the pronounced hysteresis superimposed onto $\rho_{xy}^{\mathrm{u,T}}$, observed when $\mu_0 H \parallel j \parallel ab$ -plane. The temperature dependence of $\rho_{xy}^{\mathrm{u,T}}$ (Figs. 3e-3g) reveals not only an important increase in the irreversibility field $\mu_0 H_c^{ab}(\theta = 90^\circ)$ (vertical red

arrows) as T is lowered, but a broad maximum whose amplitude and field width (color shaded areas) is T-dependent. Here, we emphasize that i) great care was taken to carefully align the field along the direction of the electrical current, and ii) the behavior of $\rho_{xy}^{u,T}(\mu_0 H)$, namely the presence of a broad peak, bears no resemblance to the behavior of either the magnetization (Figure S1) or the longitudinal magnetoresistivity (Figure S4). For example, neither the magnetization, nor the longitudinal magnetoresistivity, displays a zero value above $\mu_0 H \sim 6$ T at T = 200 K. This indicates that $\rho_{xy}^{u,T}(\mu_0 H)$ cannot be attributed to an AHE component due to simple sample misalignment. This is further confirmed by data collected on crystals having t = 15 nm and 30 nm, which displays a very small $\rho_{xy}^{u,T}(\mu_0 H)$ signal at T = 240 K, while still exhibiting a sizeable AHE response (Figure S5). Instead, as argued in Refs.^{32, 36}, this corresponds to an unconventional THE response (i.e., unconventional measurement geometry) resulting from magnetic field-induced chiral spin textures that bend the electronic orbits and induce a Hall-like response. Our results imply that these textures are affected not only by temperature, and, hence, the magneto-structural transition at $T_s \sim 110 \text{ K}$, but also by thickness and/or the geometry of the exfoliated crystals that affects the magnetic anisotropy and the relative strength between dipolar and exchange interactions. In contrast, point disorder is clearly detrimental to $\rho_{xy}^{u,T}$ as can be seen in Fig. 3c for (Fe_{0.85}Ni_{0.15})_{5-x}GeTe₂ which reveals no evidence of the unconventional topological Hall response for fields nearly along the abplane. Albeit, this compound still exhibits basically the same maximum amplitude for the anomalous Hall response relative to the undoped compound.

Remnant unconventional topological Hall response and Lorentz TEM images

To illustrate this point, we carefully measured $\rho_{xy}^{u,T}$ in four exfoliated crystals, with thicknesses of t = 12 nm, 15 nm, 30 nm, and 50 nm, as a function of $\mu_0 H \parallel j \parallel ab$ -plane, for several temperature

values (Figure 4). All samples display a very pronounced, anti-symmetric, and hysteretic Tdependent signal that leads to coercive fields as large as $\mu_0 H_c^{ab} \sim 5.65$ T, in contrast to $\mu_0 H_c^c \sim 0.2$ T (for the t = 30 nm thick sample at T = 40 K).

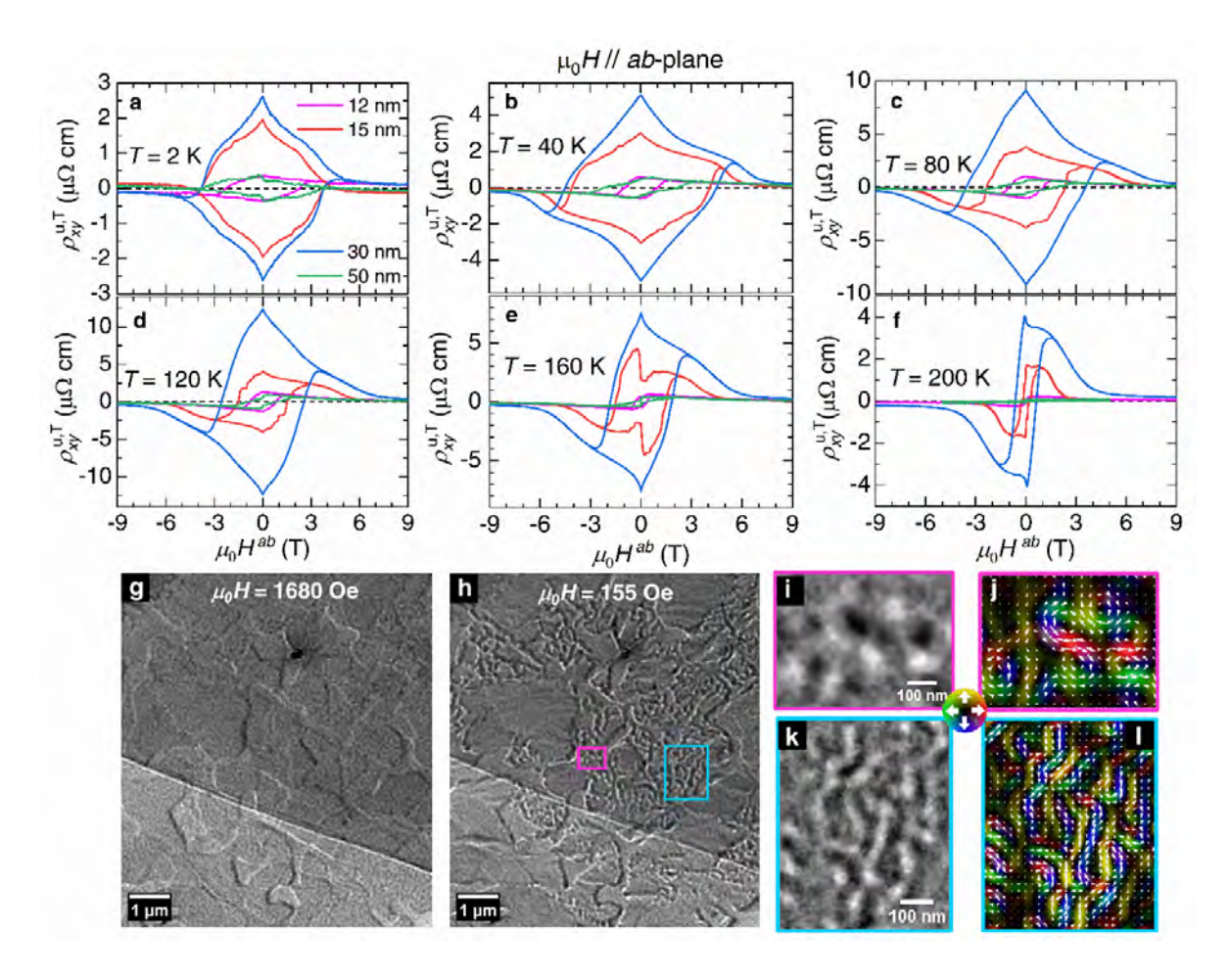


Figure 4. Hysteretic Hall-like response along the planar direction and remnant chiral spin textures. (a-f) Unconventional THE response for four samples having different thickness, t, as a function of $\mu_0 H$ aligned parallel to the electrical current flowing within the ab-plane, for T=2 K, 40 K, 80 K, 120 K, 160 K, and 200 K, respectively. Magenta, red, blue, and green traces correspond to samples with t=12 nm, 15 nm, 30 nm, and 50 nm, respectively. Notice the increase in $\mu_0 H_c^{ab}$ as T decreases, and the observation of a broad peak beyond $\mu_0 H_c^{ab}$ (see, Figs. 3e – 3g) which displays a maximum value for 120 K $\leq T \leq$ 160 K. Both the reversible and irreversible components of this unconventional Hall response are largest for the sample with thickness t=30 nm. (g) LTEM image of an exfoliated Fe_{5-x}GeTe₂ crystal encapsulated with a graphene layer (darker region) in

an out-of-plane field of $\mu_0 H = 1680$ Oe. Under this field, the mgnetic domains are polarized. (h) LTEM image of the same region in the remnant field out-of-plane field of the objective lens ($\mu_0 H \sim 155$ Oe), revealing labyrinthine domains (area enclosed by blue rectangle) as well as skyrmions (magenta rectangle). To image Néel-like out-of-plane domains, for both panels g and h, the sample was tilted by 25° about the x-axis. (i-j) Magnified image and magnetic induction map, reconstructed using the transport of intensity equation⁴³ respectively, of the area enclosed by the magenta rectangle. This reveals the projected component of magnetic induction of the inner and outer regions in Néel skyrmions, showing a bound vortex / anti-vortex structure. Colors correspond to the in-plane orientation of the local magnetization. (k-l) Labyrinthine domains and corresponding magnetic induction maps for the area enclosed by the blue rectangle.

Most importantly, this hysteresis leads to pronounced T- and field-sweep-orientation-dependent remnant values for $\rho_{xy}^{\rm u,T}$ ($\mu_0 H=0$ T) or $\rho_{xy}^{\rm u,T,rem}\cong 12.5~\mu\Omega$ cm for the t=30 nm sample at 120 K. This hysteresis in $\rho_{xy}^{u,T}$ it is not observed in the longitudinal magnetoresistivity (Figure S4) for T > 100 K. Furthermore, for all temperatures the longitudinal magnetoresistivity always returns to its original zero-field value after sweeping the magnetic field along either direction. This implies that ferromagnetic domain wall pinning, and field-induced domain wall reconfiguration, are not the main mechanisms leading to hysteresis. Domain walls are barriers for carrier motion and are reported to affect the resistivity in many systems 44-48 leading to hysteresis. In contrast, and as seen through Figs. 4 to 4f, $\rho_{xy}^{u,T}$ increases continuously as the field is reduced to zero, implying that the magnetic structures responsible for it are not pinned, as conventional FM domain walls, but evolve continuously as a function of decreasing magnetic field. Therefore, the hysteresis seen solely in $\rho_{xy}^{u,T}$, and leading to a finite Hall-like response at zero magnetic field, ought to result from remnant magnetic field-induced chiral spin textures, such as merons, upon field removal. This assertion is supported by our LTEM results on exfoliated samples of Fe_{5-x}GeTe₂ (Figs. 4g-4l). LTEM is a powerful magnetic domain visualization technique with sub-micron resolution, or higher resolution then magneto-optical Kerr effect, being comparable to near field probes⁴⁹, although being sensitive to the component of the magnetization perpendicular to the electron beam. We observed that spin textures (e.g., skyrmions and merons) remain after the external magnetic field has increased to the point of completely removing their presence and has been subsequently reduced to the lowest values attainable within the LTEM instrument (Fig. 4h). Our micromagnetic simulations indicate that the largest density of magnetic textures, and, hence, largest topological charge density is observed at $\mu_0 H = 0$ T (Figure S6). An increasing in-plane field suppresses the spin textures, especially merons, as the exchange energy forces them to transition to saturated spin configurations (stripe domains). In Figure 3, one can see that the broad reversible peaks observed in $\rho_{xy}^{u,T}$ beyond the irreversibility field H_c^{ab} , display maximum values in the temperature range ~80 K to ~160 K, precisely in the temperature range where the hysteresis becomes most pronounced (despite its absence in the longitudinal MR), leading to the largest values of $\rho_{xy}^{\text{u,T,rem}}$ and, thus, implying a correlation with $\rho_{xy}^{u,T}$. Note that a Hall effect at zero field is not the exclusive purview of the quantum AHE⁵⁰⁻⁵², but has also been observed in a compound characterized by chiral, albeit, dynamical spin-ice configurations^{53, 54}. Note also that the values of $\rho_{xy}^{u,T,max}(t=30 \text{ nm})$ approach the maximum values of the colossal THE55 observed in MnBi₄Te₇, while $\rho_{xy}^{\text{u,T,rem}}$ surpasses them. $\rho_{xy}^{u,T,rem}$ cannot be ascribed to defects, since it is difficult to understand how defects could lead to behavior that is field orientation dependent or would lead to well oriented magnetic moments at zero field (i.e., mimicking ferromagnetism) as to provide a global Hall response at zero field. Finally, we point out that $\rho_{xy}^{u,T}(\mu_0 H)$ changes its sign at either side of θ = 90°, suggesting that spin textures are written by the out-of-the-plane component of the magnetic field (Figure S7). We found that it is quite difficult to align the field very carefully within the abplane (*i.e.*, with a misalignment inferior to $\Delta\theta \sim 0.05^{\circ}$) and in this way detect $\rho_{xy}^{u,T}(\mu_0 H) = 0 \ \mu\Omega$ cm. Our micromagnetic simulations^{36, 56, 57} mimicking an exfoliated sample (Fig. S8), yields a topological charge density as a function of the interlayer magnetic field which displays a striking resemblance with the topological Hall response shown in Fig. 4. The Hall resistance R_{xy} is proportional to the topological number N_{Sk} via $R_{xy} \propto \int_{-y_0}^{y_0} \int_{-x_0}^{x_0} N_{Sk}(x-x',y-y') dx' dy'$ ⁵⁸, which is related to the emergent field created by the spin textures via $\mathbf{B}_{em} \propto N_{Sk} \hat{e}_z$ ⁵⁹. Therefore, the topological Hall resistance is directly proportional to the emergent field induced by the spin textures and associated topological charge density due to the presence of skyrmions and merons.

We provide a summary of the irreversible fields as well as the amplitudes for both the AHE and the unconventional THE responses in Figure 5. The data for four sample thicknesses that are well beyond the monolayer limit suggest that thicker crystals display larger values of H_c^c s for magnetic fields applied perpendicular to the layers (Fig. 5a) than thinner crystals²⁹. As for H_c^{ab} , seemingly the thinnest flakes display the smallest values (Fig. 5b), suggesting the evolution of the spin textures as a function of $t^{33, 34}$. However, both ρ_{xy}^A and $\rho_{xy}^{u,T}$ display a pronounced thickness dependence despite the multilayered nature of the measured crystals (Fig. 5c-5d). Given that ρ_{xy}^A in Fe_{5-x}GeTe₂ is dominated by the intrinsic contribution, as shown in Fig. 1 and related discussion, thickness-dependent values for ρ_{xy}^A indeed support the notion of spin textures evolving as a function of sample thickness. For instance, in Fig. 5c the maximum values of ρ_{xy}^A , observed at $T \approx 130$ K for both the t = 30 nm and t = 12 nm samples, are 22.6 $\mu\Omega$ cm and 1.76 $\mu\Omega$ cm, respectively. This is a broad range of values that contrasts markedly with the reproducibility of the bulk value^{20,36}, *i.e.*, $\rho_{xy}^A \sim 4.5$ to 6.3 $\mu\Omega$ cm.

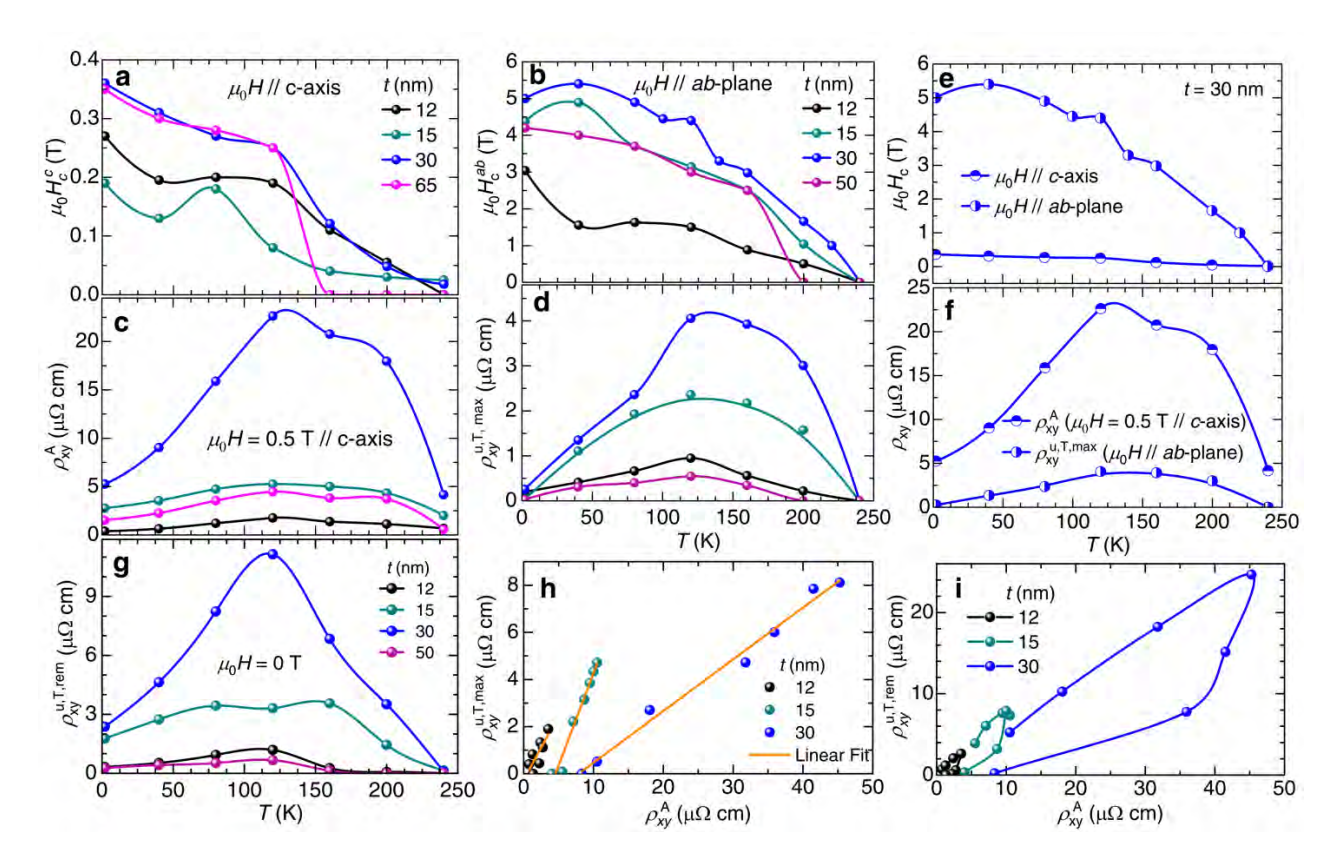


Figure 5. Correlating coercive fields, anomalous and unconventional topological Hall signals as a function of thickness. (a-b) Coercivity fields $\mu_0 H_c^c$ and $\mu_0 H_c^{ab}$, respectively, as functions of temperature (T) for five samples with thicknesses of 12 nm (black), 15 nm (green), 30 nm (blue), 50 nm (purple), and 65 nm (magenta). (c) Anomalous Hall resistivity ρ_{xy}^A under $\mu_0 H = 0.5$ T applied along the c-axis. For all thicknesses, ρ_{xy}^A increases as T decreases, reaching a maximum value just above the magnetostructural transition at $T_s \sim 110$ K. (d) Amplitude of the maximum $\rho_{xy}^{u,T,max}$ observed beyond $\mu_0 H_c^{ab}$ in the antisymmetric planar Hall-like response of topological character. For all four samples $\rho_{xy}^{u,T,max}$ peaks just above T_s , with the t=30 nm sample displaying the most pronounced response over the entire T range. e, H_c^c and H_c^{ab} as functions of T for the t=30 nm sample. (f) Comparison between the temperature dependences of $\rho_{xy}^A(\mu_0 H = 0.5$ T) and $\rho_{xy}^{u,T,max}$ for the t=30 nm sample, revealing that both variables peak around T_s albeit decreasing as T is lowered. (g) Remnant value of the unconventional topological Hall response $\rho_{xy}^{u,T,rem} = \rho_{xy}^{u,T}(\mu_0 H = 0$ T) as a function of T and for all four sample thicknesses. Note that $\rho_{xy}^{u,T,rem}$ also displays a maximum around the same temperature ($T \sim 120$ K) where maxima are observed in both ρ_{xy}^A and $\rho_{xy}^{u,T}$. (h) Amplitude of the peak $\rho_{xy}^{u,T,max}$ observed in $\rho_{xy}^{u,T}$ beyond $\mu_0 H_c^{ab}$

as a function of ρ_{xy}^A . One observes a linear relation (orange lines are linear fits) between both quantities, despite the different field orientations used to measure each variable, implying that both are driven by the same underlying physics. i, $\rho_{xy}^{\text{u,T,rem}}$ as a function of ρ_{xy}^A for the different samples revealing a nearly linear relation until the magneto-structural transition is reached, from which point $\rho_{xy}^{\text{u,T,rem}}$ decreases steeply.

Two additional and important aspects should be considered: Firstly, the suppression of both ρ_{xy}^{A} and $\rho_{xy}^{u,T}$ (Figs. 5c-5d) upon cooling below the magnetostructural transition at $T_s \sim 110$ K, with the former remaining finite and the latter approaching zero at the lowest temperatures. Secondly, the scaling of $\rho_{xy}^{u,T}$ with ρ_{xy}^A suggesting that $\rho_{xy}^{u,T}$ is also driven by the intrinsic contribution. This is supported by the behavior of $\rho_{xy}^{u,T,rem}$ as a function of t and T (Fig. 5g), which mimics that of $\rho_{xy}^{A}(t,T)$, and the linear scaling between $\rho_{xy}^{u,T.max}$ and $\rho_{xy}^{A}(t,T)$ (Fig. 5h) despite the orthogonality in field orientations used to measure the two quantities. We also observe an almost linear relation between $\rho_{xy}^{u,T,rem}$ and $\rho_{xy}^{A}(t,T)$ for $T > T_s$ implying that the intrinsic, topological charge dominated mechanism, leads to the sizeable values of $\rho_{xy}^{u,T,rem}$ (Fig. 5i). Finally, the samples displaying the largest values for both $ho_{xy}^{\mathrm{u,T,max}}$ and ho_{xy}^{A} are also the ones exhibiting the largest coercive fields $\mu_0 H_c^c$ and $\mu_0 H_c^{ab}$ (Figs. 5e-5f for t = 30 nm). This confirms that the relative change in the values of the exchange constants, magnetic axial anisotropy, and dipolar interactions favors more robust chiral textures with respect to the application of an external magnetic field. These chiral spin textures should affect the Berry phase of the charge carriers in both real and reciprocal spaces, to yield the anomalous and unconventional topological Hall responses²⁷ as reported here. Although the spin textures for magnetic fields applied along the c-axis have been studied via LTEM^{20, 21, 33,} ³⁶, their presence and evolution as a function of temperature and fields applied in plane remains to be investigated. Notice that an analysis of the conventional THE as a function of both the

magnetization and magnetoresistivity, is not possible in exfoliated flakes, given the impossibility of accurately measuring their absolute magnetization. In contrast, the unconventional THE is not masked by a superimposed AHE component and conveniently exposing solely the topological contribution.

CONCLUSIONS

In exfoliated Fe_{5-x}GeTe₂, in-plane coercive fields exceed, by more than one order of magnitude, those for fields applied perpendicularly to the planes, as well as those reported for its sister compound Fe_{3-x}GeTe₂. In relatively thick multilayered flakes that would be expected to display bulk behavior, both the anomalous Hall and unconventional topological Hall responses are strongly thickness dependent. This suggests that both Hall signals have a similar origin, i.e., the exfoliation tuning of the relative strengths of dipolar and exchange interactions. This modulation affects the stability and, hence, the density of chiral spin textures affecting the Berry phase of the moving charge carriers in real and reciprocal spaces. This is supported by a scaling analysis of the anomalous Hall-effect of Fe_{5-x}GeTe₂ indicating that it is dominated by the intrinsic Berry phase contribution. The unconventional THE displays a sizeable remnant value at zero-field and at temperatures for which the magnetoresistivity displays no hysteresis. This indicates that the hysteresis, and the finite zero-field Hall-like response, result from remnant, field-induced chiral spin textures with a well-defined dominant chirality, or topological charge. This is supported by our LTEM study in Fe_{5-x}GeTe₂ and the micromagnetic simulations which reveal the suppression of planar ferromagnetic domains upon increasing the in-plane magnetic field, but the remanence of skyrmions upon field removal. The largest density of merons, at the vertex between planar ferromagnetic domains, is found precisely at zero field. Hysteresis and remanence results from a

stable imbalance between positively- and negatively-topologically-charged spin textures leading to a hitherto unreported topological Hall effect at zero field, which is strongly thickness dependent. Several important aspects of our study remain to be understood, like to the suppression of both anomalous and topological Hall responses upon reducing the temperature below $T \sim 120$ K. This will require a detailed study on the evolution of the spin textures as a function of T < 120 K. Another quite intriguing aspect, is the observation of a pronounced topological Hall response under planar fields in the order of several tesla, since all spin textures have been suppressed when similarly intense fields were applied along the c-axis. Intense magnetic fields pose a major technical challenge for available magnetic domain imaging techniques. The important aspect is that our observations indicate that exfoliated Fe_{5-x}GeTe₂ provides a platform for the writing and electrical detection of topological spin textures aiming at energy-efficient devices based on vdW ferromagnets. In effect, topological spin textures have been proposed for the development of several computational schemes, ranging from neuromorphic⁶⁰, probabilistic⁶¹, temporal⁶², reconfigurable⁶³, high density reservoir computing⁶⁴ and even quantum computing^{65, 66}. They were also proposed for the development of memory elements^{67, 68}, such as skyrmion race tracks⁶⁹. Some of these schemes rely on magnetic tunnel junctions to detect the presence of skymions and/or current pulses to write/delete them. Here, we showed that their presence can be detected via a simple Hall response, even in absence of an external magnetic field, or that a modest external field, and in particular its orientation, can be used to write specific topological spin textures in thin van der Waals ferromagnets that can be grown in large area⁷⁰. Furthermore, remnant spin textures, in absence of an external magnetic field, provide a potential for the development of non-volatile information carriers, whose spin textures can be controlled via global or local magnetic fields. This, coupled with the simple methods described here to write and detect skymions, unveils the

potential of van der Waals ferromagnets for applications. It remains to be seen if this effect can be brought to room temperature *via* Ni or Co doping, which is known to increase its Curie temperature.

METHODS/EXPERIMENTAL

Single-crystal synthesis. Single crystals of Fe_{5-x}GeTe₂ were synthesized through a chemical vapor transport technique. Starting molar ratios of 6.2:1:2 for Fe, Ge, and Te, respectively, were loaded into an evacuated quartz ampoule with approximately 100 mg of I₂ acting as the transport agent. After the initial warming, a temperature gradient of 75°C was established between a 775 °C and 700 °C zone of a 2-zone furnace and maintained for 14 days, during which large single crystals nucleated at the 700°C zone. Samples were subsequently quenched in ice water to yield the maximum Curie temperature¹¹. Crystals used in this paper are from the same batch used in previous experiments⁷¹. Crystals were washed in acetone and subsequently isopropyl alcohol to remove residual iodine from their surface. According to Energy Dispersive Spectroscopy, the values of *x* are found to range between 0.15 and 0.

Single-Crystal X-ray diffraction. The crystal structure of Ni doped Fe_{5-x}GeTe₂ was determined using a single crystal fragment on a Bruker D8 Quest Kappa single crystal X-ray diffractometer equipped with an I μ S microfocus source (Mo K $_{\alpha}$ λ = 0.71073 Å), HELIOS optics monochromator, and PHOTON III CPAD detector. Diffraction data was integrated using the Bruker SAINT program and an absorption correction was applied to the intensities with a multi-scan method in SADABS 2016/2. A preliminary starting model was obtained using the intrinsic phasing method in SHELXT. Our best fit model resulted in the crystallographic structure $R\bar{3}m$ and cell dimensions of a = 4.037(4) Å, and c = 29.11(4) Å; additional reflections were observed in the hk1plane and were not indexed in final model. As Ni and Fe are indistinguishable via X-ray diffraction, energy dispersive spectroscopy values of Fe_{3.95}Ni_{0.67}GeTe₂ were used to constrain structure occupation factors of Fe and Ni yielding a composition of Fe_{4.01}Ni_{0.68} GeTe₂.

Table 1 Crystallographic Data and Refinement Parameters of Fe_{4.01}Ni_{0.68}GeTe₂

Empirical Formula	$Fe_{4.01}Ni_{0.68}GeTe_2$		
Space group, crystal system	<i>R</i> 3 <i>m</i> :H		
Lattice Parameters			
a (Å)	4.037 (4)		
c (Å)	29.11 (4)		
Volume [ų]	410.8(1)		
Z	1		
Density [g/cm ³]	7.177		
Absorption coefficient [mm ⁻¹]	28.34		
F(000)	778		
Crystal size [mm ³]	$0.05\times0.04\times0.02$		
θ range [°]	2.1-28.3		
Index range			
h	-5→5		
k	-5→5		
l	-37→37		
Number of reflections	3059		
Unique reflections	166		
Parameters/restraints	17/0		
R_{int}	0.068		
$\Delta ho_{max/min}$	1.95/-2.27		
GoF	1.24		
$R [F^2 > 2\sigma(F^2)]$	0.036		
$wR_2(F^2)$	0.085		
$R = \sum (F_o - F_c) / \sum F_o \text{ and } wR_2 = \{\sum w[(F_o)^2 - (F_c)^2]^2 / \sum w[(F_o)^2]^2\}^{1/2}$			

Table S1 and **Figure S3** in the Slist atomic coordinates and display Bragg reflections used for the X-ray refinement of the crystallographic structure, respectively.

Electrical transport measurements. To prevent oxidation, single crystals were exfoliated under argon atmosphere, within a glove box containing less than 10 parts per billion in oxygen, and water vapor. These were subsequently dry transferred onto Ti:Au contacts pre-patterned on a SiO_2/p -Si wafer using a polydimethylsiloxane stamp, and subsequently encapsulated among h-BN layers, with both operations performed under inert conditions. Titanium and gold layers were deposited via e-beam evaporation techniques, and electrical contacts fabricated through electron beam lithography. All measurements were performed in a Quantum Design Physical Property Measurement System.

Cryogenic Lorentz transmission electron microscopy. Single crystalline Fe_{5-x}GeTe₂ was mechanically exfoliated directly onto homemade polydimethylsiloxane stamp inside an argon filled glovebox. Prior to its

utilization, the stamp was rinsed in acetone and isopropyl alcohol to clean its surface. After appropriate crystal thicknesses and dimensions were identified *via* optical contrast, the selected crystal(s) was transferred onto a window of a silicon-nitride based transmission electron microscopy grid. Few-layer graphite (14 nm thick) was transferred onto the Fe_{5-x}GeTe₂ flake through the same dry transfer method to protect the sample from oxidization. To characterize the magnetic domains, the out-of-focus LTEM images were taken in a JEOL 2100F TEM operating in Lorentz mode (Low Mag), a perpendicular magnetic field aligned parallel to electron beams being generated by applying a small amount of current to the objective lens. The magnetic induction maps were reconstructed based on transport-of-intensity equation (TIE) method using the PyLorentz software package⁴³.

Micromagnetic Simulations. The numerical simulations were performed using the Mumax3 solver⁷², which allowed larger simulation sizes relatively to atomistic spin dynamics^{57, 73-8269-80}. Regions of in-plane and out-of-plane anisotropy comprised of Thiessen polygons were generated with Voronoi tessellation, using a grain size of 200 nm. The material parameters were chosen to be¹⁹ exchange constant $A = 10 \text{ pJ m}^{-1}$, Gilbert damping $\alpha = 0.3$, saturation magnetisation $M_s = 630 \text{ kA m}^{-1}$ along c-axis, $M_s = 730 \text{ kA m}^{-1}$ along ab-plane, $D = 1.2 \text{ mJ m}^{-2}$ and $K_u = 2.5 \text{ kJ m}^{-3}$ in the out-of-plane regions, and periodic boundary conditions were applied in the lateral film dimensions. The magnetization was initially randomized before relaxing the magnetic material in the presence of a $+\hat{z}$ directed magnetic field, before being reduced to zero-field. For hysteresis calculations, the external field was applied in-plane and varied in steps of 10 Oe, and the average topological charge density was recorded as a function of in-plane field at each step. The simulations were performed with a grid resolution of 2 nm to ensure sufficient accuracy in the topological charge calculations.

ASSOCIATED CONTENT

Supporting Information

Magnetic response of bulk single-crystalline Fe_{5-x}GeTe₂, transverse magnetoresistivity MR as a function of the magnetic field μ_0H applied along the c-axis of a 15 nm thick Fe_{5-x}GeTe₂ crystal and for several temperatures, atomic coordinates of Fe_{4.01}Ni_{0.68}GeTe₂ from single crystal X-ray diffraction, single crystal X-ray diffraction of Fe_{4.01}Ni_{0.68}GeTe₂, longitudinal magnetoresistivity MR ($\mu_0H \parallel j$ with j being the current density) as a function of the magnetic field μ_0H applied along the c-axis of a 15 nm thick Fe_{5-x}GeTe₂ crystal and for several temperatures, hysteretic response in both the anomalous Hall and unconventional topological Hall response of exfoliated Fe_{5-x}GeTe₂ crystals, topological charge density as a function of the magnetic field according to micromagnetic simulations, unconventional topological Hall response for fields very close to the ab-plane, calculation of the topological charge as a function of the inter-planar magnetic field, parameters used for the micromagnetic simulations.

The Supporting Information is available free of charge at https://pubs.acs.org/doi/

Corresponding authors

Luis Balicas - ¹National High Magnetic Field Laboratory, Tallahassee, FL 32310, USA. 2Department of Physics, Florida State University, Tallahassee, USA. https://orcid.org/0000-0002-5209-0293, Email: lbalicas@fsu.edu

Elton J. G. Santos – Institute for Condensed Matter and Complex Systems, School of Physics and Astronomy, The University of Edinburgh, EH9 3FD, UK. [†]Higgs Centre for Theoretical Physics, The University of Edinburgh, EH9 3FD, UK. https://orcid.org/0000-0001-6065-5787, Email: esantos@ed.ac.uk

AUTHOR CONTRIBUTIONS

A.M. and W.Z. fabricated the heterostructures under inert conditions. A.M. performed the transport measurements. Y.L. and C.P. performed the L-TEM study and analysis. B.W.C. and J. M. grew and characterized the Fe_{5-x}GeTe₂ bulk single-crystals. C.M. and E.J.G.S. performed the micromagnetic simulations, and the theoretical description of the data. M.B. performed the X-ray diffraction of the (Fe_{0.85}Ni_{0.15})_{5-x}GeTe₂ single crystals, and analyzed the results with G.T.M., and J.Y.C. L.B. wrote the manuscript with input from all co-authors. All authors read the manuscript, commented on it, and have given their approval to the final version.

ACKNOWLEDGEMENTS

L.B. acknowledges support from the US DoE, BES program through award DE-SC0002613 US (synthesis and measurements), US-NSF-DMR 2219003 (heterostructure fabrication) and the Office Naval Research DURIP Grant 11997003 (stacking under inert conditions). J.Y.C acknowledges NSF DMR-2209804 and the Welch Foundation through AA-2056-20220101. The National High Magnetic Field Laboratory acknowledges support from the US-NSF Cooperative agreement Grant numbers DMR-1644779 and DMR-2128556, and the state of Florida. EJGS acknowledges computational resources through CIRRUS Tier-2 HPC Service (ec131 Cirrus Project) at EPCC (http://www.cirrus.ac.uk) funded by the University of Edinburgh and EPSRC (EP/P020267/1); ARCHER UK National Supercomputing Service (http://www.archer.ac.uk) via Project d429. EJGS acknowledges the EPSRC Open Fellowship (EP/T021578/1) and the Edinburgh-Rice Strategic Collaboration Awards for funding support. Work at Argonne (Y.L, C.P) was funded by the US Department of Energy, Office of Science, Office of Basic Energy Sciences, Materials Science and Engineering Division. Use of the Center for Nanoscale Materials, an Office of Science user facility, was supported by the U.S. Department of Energy, Office of Science, Office of Basic Energy Sciences, under Contract No. DE-AC02-06CH11357.

REFERENCES

- (1) Wang, Q. H.; Bedoya-Pinto, A.; Blei, M.; Dismukes, A. H.; Hamo, A.; Jenkins, S.; Koperski, M.; Liu, Y.; Sun, Q.-C.; Telford, E. J.; et al. The Magnetic Genome of Two-Dimensional van der Waals Materials. *Acs Nano* **2022**, *16* (5), 6960-7079. DOI: 10.1021/acsnano.1c09150.
- (2) Gibertini, M.; Koperski, M.; Morpurgo, A. F.; Novoselov, K. S. Magnetic 2D materials and heterostructures. *Nat. Nanotechnol.* **2019**, *14* (5), 408-419. DOI: 10.1038/s41565-019-0438-6.
- (3) Jiang, X.; Liu, Q. X.; Xing, J. P.; Liu, N. S.; Guo, Y.; Liu, Z. F.; Zhao, J. J. Recent progress on 2D magnets: Fundamental mechanism, structural design and modification. *Appl. Phys. Rev.* **2021**, 8 (3). DOI: 10.1063/5.0039979.
- (4) Huang, B.; Clark, G.; Navarro-Moratalla, E.; Klein, D. R.; Cheng, R.; Seyler, K. L.; Zhong, D.; Schmidgall, E.; McGuire, M. A.; Cobden, D. H.; et al. Layer-dependent ferromagnetism in a van der Waals crystal down to the monolayer limit. *Nature* **2017**, *546* (7657), 270. DOI: 10.1038/nature22391.
- (5) Fei, Z.; Huang, B.; Malinowski, P.; Wang, W.; Song, T.; Sanchez, J.; Yao, W.; Xiao, D.; Zhu, X.; May, A. F.; et al. Two-dimensional itinerant ferromagnetism in atomically thin Fe₃GeTe₂. *Nat Mater* **2018**, *17* (9), 778-782. DOI: 10.1038/s41563-018-0149-7.
- (6) Jiang, S.; Shan, J.; Mak, K. F. Electric-field switching of two-dimensional van der Waals magnets. *Nat. Mater.* **2018**, *17* (5), 406-410. DOI: 10.1038/s41563-018-0040-6.
- (7) Burch, K. S.; Mandrus, D.; Park, J.-G. Magnetism in two-dimensional van der Waals materials. *Nature* **2018**, *563* (7729), 47-52. DOI: 10.1038/s41586-018-0631-z.
- (8) Deiseroth, H.-J.; Aleksandrov, K.; Reiner, C.; Kienle, L.; Kremer, R. K. Fe₃GeTe₂ and Ni₃GeTe₂ Two fir Layered Transition-Metal Compounds: Crystal Structures, HRTEM Investigations, and Magnetic and Electrical Properties. *Eur. J. Inorg. Chem.* **2006**, *2006* (8), 1561-1567. DOI: https://doi.org/10.1002/ejic.200501020.
- (9) Zhang, B.; Zeng, Y.; Zhao, Z.-J.; Qiu, D.-P.; Zhang, T.; Hou, Y.-L. Magnetic two-dimensional chromium trihalides: structure, properties and modulation. *Rare Met.* **2022**, *41* (9), 2921-2942. DOI: 10.1007/s12598-022-02004-2.
- (10) Seo, J.; Kim, D. Y.; An, E. S.; Kim, K.; Kim, G.-Y.; Hwang, S.-Y.; Kim, D. W.; Jang, B. G.; Kim, H.; Eom, G.; et al. Nearly room temperature ferromagnetism in a magnetic metal-rich van der Waals metal. *Sci. Adv.* **2020**, *6* (3), eaay8912. DOI: 10.1126/sciadv.aay8912.
- (11) May, A. F.; Ovchinnikov, D.; Zheng, Q.; Hermann, R.; Calder, S.; Huang, B.; Fei, Z. Y.; Liu, Y. H.; Xu, X. D.; McGuire, M. A. Ferromagnetism Near Room Temperature in the Cleavable van der Waals Crystal Fe₅GeTe₂. *ACS Nano* **2019**, *13* (4), 4436-4442. DOI: 10.1021/acsnano.8b09660.
- (12) Chen, X.; Shao, Y.-T.; Chen, R.; Susarla, S.; Hogan, T.; He, Y.; Zhang, H.; Wang, S.; Yao, J.; Ercius, P.; et al. Pervasive beyond Room-Temperature Ferromagnetism in a Doped van der Waals Magnet. *Phys. Rev. Lett.* **2022**, *128* (21), 217203. DOI: 10.1103/PhysRevLett.128.217203.
- (13) Deng, Y.; Yu, Y.; Song, Y.; Zhang, J.; Wang, N. Z.; Sun, Z.; Yi, Y.; Wu, Y. Z.; Wu, S.; Zhu, J.; et al. Gate-tunable room-temperature ferromagnetism in two-dimensional Fe₃GeTe₂. *Nature* **2018**, *563* (7729), 94-99. DOI: 10.1038/s41586-018-0626-9.
- (14) Tan, C.; Xie, W.-Q.; Zheng, G.; Aloufi, N.; Albarakati, S.; Algarni, M.; Li, J.; Partridge, J.; Culcer, D.; Wang, X.; et al. Gate-Controlled Magnetic Phase Transition in a van der Waals Magnet Fe₅GeTe₂. *Nano Lett.* **2021**, *21* (13), 5599-5605. DOI: 10.1021/acs.nanolett.1c01108.
- (15) Zheng, G.; Xie, W.-Q.; Albarakati, S.; Algarni, M.; Tan, C.; Wang, Y.; Peng, J.; Partridge, J.; Farrar, L.; Yi, J.; et al. Gate-Tuned Interlayer Coupling in van der Waals Ferromagnet Fe₃GeTe₂ Nanoflakes. *Phys. Rev. Lett.* **2020**, *125* (4), 047202. DOI: 10.1103/PhysRevLett.125.047202.

- (16) Moriya, T. Anisotropic Superexchange Interaction and Weak Ferromagnetism. *Phys. Rev.* **1960**, *120* (1), 91-98. DOI: 10.1103/PhysRev.120.91.
- (17) Ding, B.; Li, Z.; Xu, G.; Li, H.; Hou, Z.; Liu, E.; Xi, X.; Xu, F.; Yao, Y.; Wang, W. Observation of Magnetic Skyrmion Bubbles in a van der Waals Ferromagnet Fe₃GeTe₂. *Nano Lett.* **2020**, *20* (2), 868-873. DOI: 10.1021/acs.nanolett.9b03453.
- (18) Schmitt, M.; Denneulin, T.; Kovács, A.; Saunderson, T. G.; Rüßmann, P.; Shahee, A.; Scholz, T.; Tavabi, A. H.; Gradhand, M.; Mavropoulos, P.; et al. Skyrmionic spin structures in layered Fe₅GeTe₂ up to room temperature. *Commun. Phys.* **2022**, *5* (1), 254. DOI: 10.1038/s42005-022-01031-w.
- (19) Casas, B. W.; Li, Y.; Moon, A.; Xin, Y.; McKeever, C.; Macy, J.; Petford-Long, A. K.; Phatak, C. M.; Santos, E. J. G.; Choi, E. S.; et al. Coexistence of Merons with Skyrmions in the Centrosymmetric Van Der Waals Ferromagnet Fe_{5-x}GeTe₂. *Adv. Mater.* 35 (n/a), 2212087. DOI: https://doi.org/10.1002/adma.202212087.
- (20) Gao, Y.; Yin, Q.; Wang, Q.; Li, Z.; Cai, J.; Zhao, T.; Lei, H.; Wang, S.; Zhang, Y.; Shen, B. Spontaneous (Anti)meron Chains in the Domain Walls of van der Waals Ferromagnetic Fe_{5-x}GeTe₂. *Adv. Mater.* **2020**, *32* (48), 2005228. DOI: https://doi.org/10.1002/adma.202005228.
- (21) Lv, X.; Pei, K.; Yang, C.; Qin, G.; Liu, M.; Zhang, J.; Che, R. Controllable Topological Magnetic Transformations in the Thickness-Tunable van der Waals Ferromagnet Fe₅GeTe₂. *ACS Nano* **2022**, *16* (11), 19319-19327. DOI: 10.1021/acsnano.2c08844.
- (22) Peng, L.; Yasin, F. S.; Park, T.-E.; Kim, S. J.; Zhang, X.; Nagai, T.; Kimoto, K.; Woo, S.; Yu, X. Tunable Néel–Bloch Magnetic Twists in Fe₃GeTe₂ with van der Waals Structure. *Adv. Funct. Mater.* **2021**, *31*, 2103583. DOI: https://doi.org/10.1002/adfm.202103583.
- (23) Lee, M.; Kang, W.; Onose, Y.; Tokura, Y.; Ong, N. P. Unusual Hall Effect Anomaly in MnSi under Pressure. *Phys. Rev. Lett.* **2009**, *102* (18). DOI: 10.1103/PhysRevLett.102.186601.
- (24) Neubauer, A.; Pfleiderer, C.; Binz, B.; Rosch, A.; Ritz, R.; Niklowitz, P. G.; Boni, P. Topological Hall Effect in the A Phase of MnSi. *Phys. Rev. Lett.* **2009**, *102* (18). DOI: 10.1103/PhysRevLett.102.186602.
- (25) Ritz, R.; Halder, M.; Franz, C.; Bauer, A.; Wagner, M.; Bamler, R.; Rosch, A.; Pfleiderer, C. Giant generic topological Hall resistivity of MnSi under pressure. *Phys. Rev. B* **2013**, *87* (13). DOI: 10.1103/PhysRevB.87.134424.
- (26) Kurumaji, T.; Nakajima, T.; Hirschberger, M.; Kikkawa, A.; Yamasaki, Y.; Sagayama, H.; Nakao, H.; Taguchi, Y.; Arima, T.-h.; Tokura, Y. Skyrmion lattice with a giant topological Hall effect in a frustrated triangular-lattice magnet. *Science* **2019**, *365* (6456), 914-918. DOI: doi:10.1126/science.aau0968.
- (27) Verma, N.; Addison, Z.; Randeria, M. Unified theory of the anomalous and topological Hall effects with phase-space Berry curvatures. *Sci. Adv.* **2022**, *8* (45), eabq2765. DOI: doi:10.1126/sciadv.abq2765.
- (28) Tian, Y.; Ye, L.; Jin, X. Proper Scaling of the Anomalous Hall Effect. *Phys. Rev. Lett.* **2009**, *103* (8), 087206. DOI: 10.1103/PhysRevLett.103.087206.
- (29) Deng, Y.; Xiang, Z.; Lei, B.; Zhu, K.; Mu, H.; Zhuo, W.; Hua, X.; Wang, M.; Wang, Z.; Wang, G.; et al. Layer-Number-Dependent Magnetism and Anomalous Hall Effect in van der Waals Ferromagnet Fe₅GeTe₂. *Nano Lett.* **2022**, *22* (24), 9839-9846. DOI: 10.1021/acs.nanolett.2c02696.
- (30) Karplus, R.; Luttinger, J. M. Hall Effect in Ferromagnetics. *Phys. Rev.* **1954**, *95* (5), 1154-1160. DOI: 10.1103/PhysRev.95.1154.

- (31) Nagaosa, N.; Sinova, J.; Onoda, S.; MacDonald, A. H.; Ong, N. P. Anomalous Hall effect. *Rev. Mod. Phys.* **2010**, *82* (2), 1539-1592. DOI: 10.1103/RevModPhys.82.1539.
- (32) Macy, J.; Ratkovski, D.; Balakrishnan, P. P.; Strungaru, M.; Chiu, Y.-C.; Savvidou, A. F.; Moon, A.; Zheng, W.; Weiland, A.; McCandless, G. T.; et al. Magnetic field-induced non-trivial electronic topology in Fe_{3-x}GeTe₂. *Appl. Phys. Rev.* **2021**, *8* (4), 041401. DOI: 10.1063/5.0052952.
- (33) Fujita, R.; Bassirian, P.; Li, Z.; Guo, Y.; Mawass, M. A.; Kronast, F.; van der Laan, G.; Hesjedal, T. Layer-Dependent Magnetic Domains in Atomically Thin Fe₅GeTe₂. *ACS Nano* **2022**, *16* (7), 10545-10553. DOI: 10.1021/acsnano.2c01948.
- (34) Zhang, H.; Raftrey, D.; Chan, Y.-T.; Shao, Y.-T.; Chen, R.; Chen, X.; Huang, X.; Reichanadter, J. T.; Dong, K.; Susarla, S.; et al. Room-temperature skyrmion lattice in a layered magnet (Fe_{0.5}Co_{0.5})₅GeTe₂. *Sci. Adv.* **2022**, *8* (12), eabm7103. DOI: 10.1126/sciadv.abm7103.
- (35) Karube, K.; Peng, L.; Masell, J.; Yu, X.; Kagawa, F.; Tokura, Y.; Taguchi, Y. Roomtemperature antiskyrmions and sawtooth surface textures in a non-centrosymmetric magnet with S4 symmetry. *Nat. Mater.* **2021**, *20* (3), 335-340. DOI: 10.1038/s41563-020-00898-w.
- (36) Casas, B. W.; Li, Y.; Moon, A.; Xin, Y.; McKeever, C.; Macy, J.; Petford-Long, A. K.; Phatak, C. M.; Santos, E. J. G.; Choi, E. S.; et al. Coexistence of Merons with Skyrmions in the Centrosymmetric Van Der Waals Ferromagnet Fe_{5-x}GeTe₂. *Adv. Mater.* **2023**, *35* (17), 2212087. DOI: https://doi.org/10.1002/adma.202212087.
- (37) Li, Z.; Liu, S.; Sun, J.; Zhu, J.; Chen, Y.; Yang, Y.; Ai, L.; Zhang, E.; Huang, C.; Leng, P.; et al. Low-pass filters based on van der Waals ferromagnets. *Nat. Electron.* **2023**, *6* (4), 273-280. DOI: 10.1038/s41928-023-00941-z.
- (38) Velický, M.; Donnelly, G. E.; Hendren, W. R.; McFarland, S.; Scullion, D.; DeBenedetti, W. J. I.; Correa, G. C.; Han, Y.; Wain, A. J.; Hines, M. A.; et al. Mechanism of Gold-Assisted Exfoliation of Centimeter-Sized Transition-Metal Dichalcogenide Monolayers. *ACS Nano* **2018**, *12* (10), 10463-10472. DOI: 10.1021/acsnano.8b06101.
- (39) Huang, Y.; Pan, Y.-H.; Yang, R.; Bao, L.-H.; Meng, L.; Luo, H.-L.; Cai, Y.-Q.; Liu, G.-D.; Zhao, W.-J.; Zhou, Z.; et al. Universal mechanical exfoliation of large-area 2D crystals. *Nat. Commun.* **2020**, *11* (1), 2453. DOI: 10.1038/s41467-020-16266-w.
- (40) Deng, Y.; Yu, Y.; Shi, M. Z.; Guo, Z.; Xu, Z.; Wang, J.; Chen, X. H.; Zhang, Y. Quantum anomalous Hall effect in intrinsic magnetic topological insulator MnBi₂Te₄. *Science* **2020**, *367* (6480), 895-900. DOI: doi:10.1126/science.aax8156.
- (41) Tan, C.; Lee, J.; Jung, S.-G.; Park, T.; Albarakati, S.; Partridge, J.; Field, M. R.; McCulloch, D. G.; Wang, L.; Lee, C. Hard magnetic properties in nanoflake van der Waals Fe₃GeTe₂. *Nat. Commun.* **2018**, *9* (1), 1554. DOI: 10.1038/s41467-018-04018-w.
- (42) Liu, E.; Sun, Y.; Kumar, N.; Muechler, L.; Sun, A.; Jiao, L.; Yang, S.-Y.; Liu, D.; Liang, A.; Xu, Q.; et al. Giant anomalous Hall effect in a ferromagnetic kagome-lattice semimetal. *Nat. Phys.* **2018**, *14* (11), 1125-1131. DOI: 10.1038/s41567-018-0234-5.
- (43) McCray, A. R. C.; Cote, T.; Li, Y.; Petford-Long, A. K.; Phatak, C. Understanding Complex Magnetic Spin Textures with Simulation-Assisted Lorentz Transmission Electron Microscopy. *Phys. Rev. Appl.* **2021**, *15* (4), 044025. DOI: 10.1103/PhysRevApplied.15.044025.
- (44) Dho, J.; Kim, W. S.; Hur, N. H. Anomalous Thermal Hysteresis in Magnetization and Resistivity of La_{1-x} Sr_xMnO₃. *Phys. Rev. Lett.* **2001**, *87* (18), 187201. DOI: 10.1103/PhysRevLett.87.187201.
- (45) Ravelosona, D.; Cebollada, A.; Briones, F.; Diaz-Paniagua, C.; Hidalgo, M. A.; Batallan, F. Domain-wall scattering in epitaxial FePd ordered alloy films with perpendicular magnetic anisotropy. *Phys. Rev. B* **1999**, *59* (6), 4322-4326. DOI: 10.1103/PhysRevB.59.4322.

- (46) Zhao, Y. M.; Mahendiran, R.; Nguyen, N.; Raveau, B.; Yao, R. H. SrFeO_{2.95} A helical antiferromagnet with large magnetoresistance. *Phys. Rev. B* **2001**, *64* (2), 024414. DOI: 10.1103/PhysRevB.64.024414.
- (47) Ando, Y.; Lavrov, A. N.; Segawa, K. Magnetoresistance anomalies in antiferromagnetic YBa₂Cu₃O_{6+x}: Fingerprints of charged stripes. *Phys. Rev. Lett.* **1999**, *83* (14), 2813-2816. DOI: 10.1103/PhysRevLett.83.2813.
- (48) Piazza, V.; Pellegrini, V.; Beltram, F.; Wegscheider, W.; Jungwirth, T.; MacDonald, A. H. First-order phase transitions in a quantum Hall ferromagnet. *Nature* **1999**, *402* (6762), 638-641. DOI: 10.1038/45189.
- (49) Marchiori, E.; Ceccarelli, L.; Rossi, N.; Lorenzelli, L.; Degen, C. L.; Poggio, M. Nanoscale magnetic field imaging for 2D materials. *Nat. Rev. Phys.* **2022**, *4* (1), 49-60. DOI: 10.1038/s42254-021-00380-9.
- (50) Chang, C.-Z.; Zhang, J.; Feng, X.; Shen, J.; Zhang, Z.; Guo, M.; Li, K.; Ou, Y.; Wei, P.; Wang, L.-L.; et al. Experimental Observation of the Quantum Anomalous Hall Effect in a Magnetic Topological Insulator. *Science* **2013**, *340* (6129), 167-170. DOI: doi:10.1126/science.1234414.
- (51) Yu, R.; Zhang, W.; Zhang, H. J.; Zhang, S. C.; Dai, X.; Fang, Z. Quantized Anomalous Hall Effect in Magnetic Topological Insulators. *Science* **2010**, *329* (5987), 61-64. DOI: 10.1126/science.1187485.
- (52) Xu, G.; Weng, H. M.; Wang, Z. J.; Dai, X.; Fang, Z. Chern Semimetal and the Quantized Anomalous Hall Effect in HgCr₂Se₄. *Phys. Rev. Lett.* **2011**, *107* (18). DOI: 10.1103/PhysRevLett.107.186806.
- (53) Machida, Y.; Nakatsuji, S.; Onoda, S.; Tayama, T.; Sakakibara, T. Time-reversal symmetry breaking and spontaneous Hall effect without magnetic dipole order. *Nature* **2010**, *463* (7278), 210-213. DOI: 10.1038/nature08680.
- (54) Balicas, L.; Nakatsuji, S.; Machida, Y.; Onoda, S. Anisotropic Hysteretic Hall Effect and Magnetic Control of Chiral Domains in the Chiral Spin States of Pr₂Ir₂O₇. *Phys. Rev. Lett.* **2011**, *106* (21). DOI: 10.1103/PhysRevLett.106.217204.
- (55) Roychowdhury, S.; Singh, S.; Guin, S. N.; Kumar, N.; Chakraborty, T.; Schnelle, W.; Borrmann, H.; Shekhar, C.; Felser, C. Giant Topological Hall Effect in the Noncollinear Phase of Two-Dimensional Antiferromagnetic Topological Insulator MnBi₄Te₇. *Chem. Mater.* **2021**, *33* (21), 8343-8350. DOI: 10.1021/acs.chemmater.1c02625.
- (56) Zhang, H.; Chen, R.; Zhai, K.; Chen, X.; Caretta, L.; Huang, X.; Chopdekar, R. V.; Cao, J.; Sun, J.; Yao, J.; et al. Itinerant ferromagnetism in van der Waals Fe_{5-x}GeTe₂ crystals above room temperature. *Phys. Rev. B* **2020**, *102* (6), 064417. DOI: 10.1103/PhysRevB.102.064417.
- (57) Iturriaga, H.; Martinez, L. M.; Mai, T. T.; Biacchi, A. J.; Augustin, M.; Hight Walker, A. R.; Sanad, M. F.; Sreenivasan, S. T.; Liu, Y.; Santos, E. J. G.; et al. Magnetic properties of intercalated quasi-2D Fe_{3-x}GeTe₂ van der Waals magnet. *npj 2D Mater. Appl.* **2023**, 7 (1), 56. DOI: 10.1038/s41699-023-00417-w.
- (58) Göbel, B.; Akosa, C. A.; Tatara, G.; Mertig, I. Topological Hall signatures of magnetic hopfions. *Phys. Rev. Res.* **2020**, *2* (1), 013315. DOI: 10.1103/PhysRevResearch.2.013315.
- (59) Göbel, B.; Schäffer, A. F.; Berakdar, J.; Mertig, I.; Parkin, S. S. P. Electrical writing, deleting, reading, and moving of magnetic skyrmioniums in a racetrack device. *Sci. Rep.* **2019**, *9* (1), 12119. DOI: 10.1038/s41598-019-48617-z.

- (60) Song, K. M.; Jeong, J.-S.; Pan, B.; Zhang, X.; Xia, J.; Cha, S.; Park, T.-E.; Kim, K.; Finizio, S.; Raabe, J.; et al. Skyrmion-based artificial synapses for neuromorphic computing. *Nat. Electron.* **2020**, *3* (3), 148-155. DOI: 10.1038/s41928-020-0385-0.
- (61) Pinna, D.; Araujo, F. A.; Kim, J. V.; Cros, V.; Querlioz, D.; Bessiere, P.; Droulez, J.; Grollier, J. Skyrmion Gas Manipulation for Probabilistic Computing. *Phys. Rev. Appl.* **2018**, *9* (6). DOI: 10.1103/PhysRevApplied.9.064018.
- (62) Vakili, H.; Sakib, M. N.; Ganguly, S.; Stan, M.; Daniels, M. W.; Madhavan, A.; Stiles, M. D.; Ghosh, A. W. Temporal Memory With Magnetic Racetracks. *IEEE J.* **2020**, *6* (2), 107-115. DOI: 10.1109/JXCDC.2020.3022381.
- (63) Luo, S.; Song, M.; Li, X.; Zhang, Y.; Hong, J.; Yang, X.; Zou, X.; Xu, N.; You, L. Reconfigurable Skyrmion Logic Gates. *Nano Lett.* **2018**, *18* (2), 1180-1184. DOI: 10.1021/acs.nanolett.7b04722.
- (64) Bourianoff, G.; Pinna, D.; Sitte, M.; Everschor-Sitte, K. Potential implementation of reservoir computing models based on magnetic skyrmions. *AIP Advances* **2018**, *8* (5), 055602. DOI: 10.1063/1.5006918.
- (65) Psaroudaki, C.; Panagopoulos, C. Skyrmion Qubits: A New Class of Quantum Logic Elements Based on Nanoscale Magnetization. *Phys. Rev. Lett.* **2021**, *127* (6). DOI: 10.1103/PhysRevLett.127.067201.
- (66) Xia, J.; Zhang, X.; Liu, X.; Zhou, Y.; Ezawa, M. Qubits based on merons in magnetic nanodisks. *Commun. Mater.* **2022**, *3* (1), 88. DOI: 10.1038/s43246-022-00311-w.
- (67) Bessarab, P. F.; Müller, G. P.; Lobanov, I. S.; Rybakov, F. N.; Kiselev, N. S.; Jónsson, H.; Uzdin, V. M.; Blügel, S.; Bergqvist, L.; Delin, A. Lifetime of racetrack skyrmions. *Sci. Rep.* **2018**, 8 (1), 3433. DOI: 10.1038/s41598-018-21623-3.
- (68) Jiang, W.; Chen, G.; Liu, K.; Zang, J.; te Velthuis, S. G. E.; Hoffmann, A. Skyrmions in magnetic multilayers. *Phys. Rep.* **2017**, 704, 1-49. DOI: https://doi.org/10.1016/j.physrep.2017.08.001.
- (69) Woo, S.; Litzius, K.; Krüger, B.; Im, M. Y.; Caretta, L.; Richter, K.; Mann, M.; Krone, A.; Reeve, R. M.; Weigand, M.; et al. Observation of room-temperature magnetic skyrmions and their current-driven dynamics in ultrathin metallic ferromagnets. *Nat. Mater.* **2016**, *15* (5), 501-506. DOI: 10.1038/nmat4593.
- (70) Ribeiro, M.; Gentile, G.; Marty, A.; Dosenovic, D.; Okuno, H.; Vergnaud, C.; Jacquot, J.-F.; Jalabert, D.; Longo, D.; Ohresser, P.; et al. Large-scale epitaxy of two-dimensional van der Waals room-temperature ferromagnet Fe₅GeTe₂. *npj 2D Mater. Appl.* **2022**, *6* (1), 10. DOI: 10.1038/s41699-022-00285-w.
- (71) Alahmed, L.; Nepal, B.; Macy, J.; Zheng, W.; Casas, B.; Sapkota, A.; Jones, N.; Mazza, A. R.; Brahlek, M.; Jin, W.; et al. Magnetism and spin dynamics in room-temperature van der Waals magnet Fe₅GeTe₂. *2D Mater.* **2021**, *8* (4), 045030. DOI: 10.1088/2053-1583/ac2028.
- (72) Vansteenkiste, A.; Leliaert, J.; Dvornik, M.; Helsen, M.; Garcia-Sanchez, F.; Waeyenberge, B. V. The design and verification of MuMax3. *AIP Adv.* **2014**, *4* (10), 107133. DOI: 10.1063/1.4899186.
- (73) Jenkins, S.; Rózsa, L.; Atxitia, U.; Evans, R. F. L.; Novoselov, K. S.; Santos, E. J. G. Breaking through the Mermin-Wagner limit in 2D van der Waals magnets. *Nat. Commun.* **2022**, *13* (1), 6917. DOI: 10.1038/s41467-022-34389-0.
- (74) Wahab, D. A.; Augustin, M.; Valero, S. M.; Kuang, W.; Jenkins, S.; Coronado, E.; Grigorieva, I. V.; Vera-Marun, I. J.; Navarro-Moratalla, E.; Evans, R. F. L.; et al. Quantum Rescaling, Domain

- Metastability, and Hybrid Domain-Walls in 2D CrI₃ Magnets. *Adv. Mater.* **2021**, *33* (5), 2004138. DOI: https://doi.org/10.1002/adma.202004138.
- (75) Augustin, M.; Jenkins, S.; Evans, R. F. L.; Novoselov, K. S.; Santos, E. J. G. Properties and dynamics of meron topological spin textures in the two-dimensional magnet CrCl₃. *Nat. Commun.* **2021**, *12* (1). DOI: 10.1038/s41467-020-20497-2.
- (76) Abdul-Wahab, D.; Iacocca, E.; Evans, R. F. L.; Bedoya-Pinto, A.; Parkin, S.; Novoselov, K. S.; Santos, E. J. G. Domain wall dynamics in two-dimensional van der Waals ferromagnets. *Appl. Phys. Rev.* **2021**, *8* (4). DOI: 10.1063/5.0062541.
- (77) Alliati, I. M.; Evans, R. F. L.; Novoselov, K. S.; Santos, E. J. G. Relativistic domain-wall dynamics in van der Waals antiferromagnet MnPS₃. *npj Comp. Mater.* **2022**, *8* (1). DOI: 10.1038/s41524-021-00683-6.
- (78) Zur, Y.; Noah, A.; Boix-Constant, C.; Mañas-Valero, S.; Fridman, N.; Rama-Eiroa, R.; Huber, M. E.; Santos, E. J. G.; Coronado, E.; Anahory, Y. Magnetic Imaging and Domain Nucleation in CrSBr Down to the 2D Limit. *Adv. Mater.* **2023**, *35* (47), 2307195. DOI: https://doi.org/10.1002/adma.202307195.
- (79) Boix-Constant, C.; Jenkins, S.; Rama-Eiroa, R.; Santos, E. J. G.; Mañas-Valero, S.; Coronado, E. Multistep magnetization switching in orthogonally twisted ferromagnetic monolayers. *Nat. Mater.* **2023**. DOI: 10.1038/s41563-023-01735-6.
- (80) Tang, C.; Alahmed, L.; Mahdi, M.; Xiong, Y.; Inman, J.; McLaughlin, N. J.; Zollitsch, C.; Kim, T. H.; Du, C. R.; Kurebayashi, H.; et al. Spin dynamics in van der Waals magnetic systems. *Phys. Rep.* **2023**, *1032*, 1-36. DOI: https://doi.org/10.1016/j.physrep.2023.09.002.
- (81) Dabrowski, M.; Guo, S.; Strungaru, M.; Keatley, P. S.; Withers, F.; Santos, E. J. G.; Hicken, R. J. All-optical control of spin in a 2D van der Waals magnet. *Nat. Commun.* **2022**, *13* (1), 5976. DOI: 10.1038/s41467-022-33343-4.
- (82) Khela, M.; Dabrowski, M.; Khan, S.; Keatley, P. S.; Verzhbitskiy, I.; Eda, G.; Hicken, R. J.; Kurebayashi, H.; Santos, E. J. G. Laser-induced topological spin switching in a 2D van der Waals magnet. *Nat. Commun.* **2023**, *14* (1), 1378. DOI: 10.1038/s41467-023-37082-y.

Supporting information for manuscript titled: "Writing and detecting topological charges in exfoliated Fe_{5-x}GeTe₂"

Alex $Moon^{\S, \ell}$, Yue Li^{α} , Conor McKeever, Brian W. Casas, Moises Bravo, Wenkai Zheng, Juan Macy, Amanda K. Petford-Long, Gregory T. McCandless, Julia Y. Chan, Charudatta Phatak, Elton J. G. Santos, and Luis Balicas, and Luis Balicas, the santos and Luis Balicas.

§National High Magnetic Field Laboratory, 1800 E. Paul Dirac Dr. Tallahassee, FL 32310, USA.

[£]Department of Physics, Florida State University, 77 Chieftan Way, Tallahassee, FL 32306, USA.

[™]Materials Science Division, Argonne National Laboratory, Lemont, 60439, IL, USA.

[‡]Institute for Condensed Matter and Complex Systems, School of Physics and Astronomy, The University of Edinburgh, EH9 3FD, UK.

¹Department of Chemistry and Biochemistry, Baylor University, Waco, TX 76798, USA.
²Department of Materials Science and Engineering, Northwestern University, Evanston, 60208, IL, USA.

[†]Higgs Centre for Theoretical Physics, The University of Edinburgh, EH9 3FD, UK.

- Figure S1. Magnetic response of bulk single-crystalline Fe_{5-x}GeTe₂.
- Figure S2. Transverse magnetoresistivity MR as a function of the magnetic field μ_0H applied along the c-axis for a 15 nm thick Fe_{5-x}GeTe₂ crystal and for several temperatures.
- Table S1. Atomic coordinates of Fe_{4.01}Ni_{0.68}GeTe₂ from single crystal X-ray diffraction
- Figure S3. Single crystal X-ray diffraction of Fe_{4.01}Ni_{0.68}GeTe₂
- Figure S4. Longitudinal magnetoresistivity MR ($\mu_0H \parallel j$ with j being the current density) as a function of the magnetic field μ_0H applied along the c-axis of a 15 nm thick Fe_{5-x}GeTe₂ crystal and for several temperatures.
- Figure S5. Hysteretic response in both the anomalous Hall and unconventional topological Hall response of exfoliated Fe_{5-x}GeTe₂ crystals.
- Figure S6. Topological charge density as a function of magnetic field according to micromagnetic simulations.
- Figure S7. Unconventional topological Hall response for fields very close to the ab-plane.
- Figure 8: Calculation of the topological charge as a function of inter-planar magnetic field.
- Table S2. Parameters used for the micromagnetic simulations.

^{*}e-mail: esantos@exseed.ed.ac.uk, balicas@magnet.fsu.edu

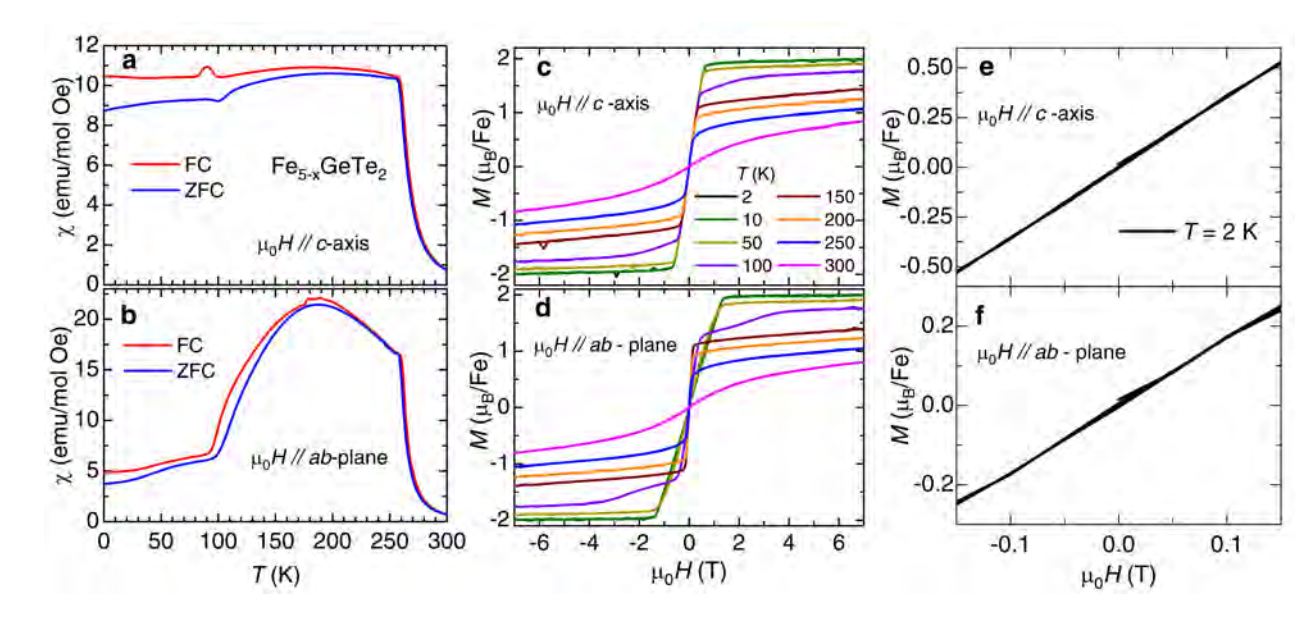


Figure S1. Magnetic response of bulk single-crystalline Fe_{5-x}GeTe₂. (a) Magnetic susceptibility χ as a function of the temperature T measured under a field $\mu_0H=100$ G applied along the c-axis of the crystal. (b) χ as a function of T for a field applied along the ab-plane. In both plots, red, and blue traces correspond to measurements performed under field-cooled and zero-field cooled conditions, respectively. The sharp increase in χ observed below T=300 K corresponds to the Curie temperature, while an anomaly is observed in the vicinity of 100 K and due to a magneto-structural transition. (c) Magnetization M as a function of the μ_0H applied along the c-axis, for several temperatures. (d) M as a function of the μ_0H applied along the ab-plane, for several temperatures. (e) M as a function of the μ_0H applied along the ab-plane shown in an amplified scale around $\mu_0H=0$ T, at T=2 K. (f) M as a function of the μ_0H applied along the ab-plane shown in an amplified scale around $\mu_0H=0$ T, at T=2 K. Notice the absence of hysteresis in bulk crystals.

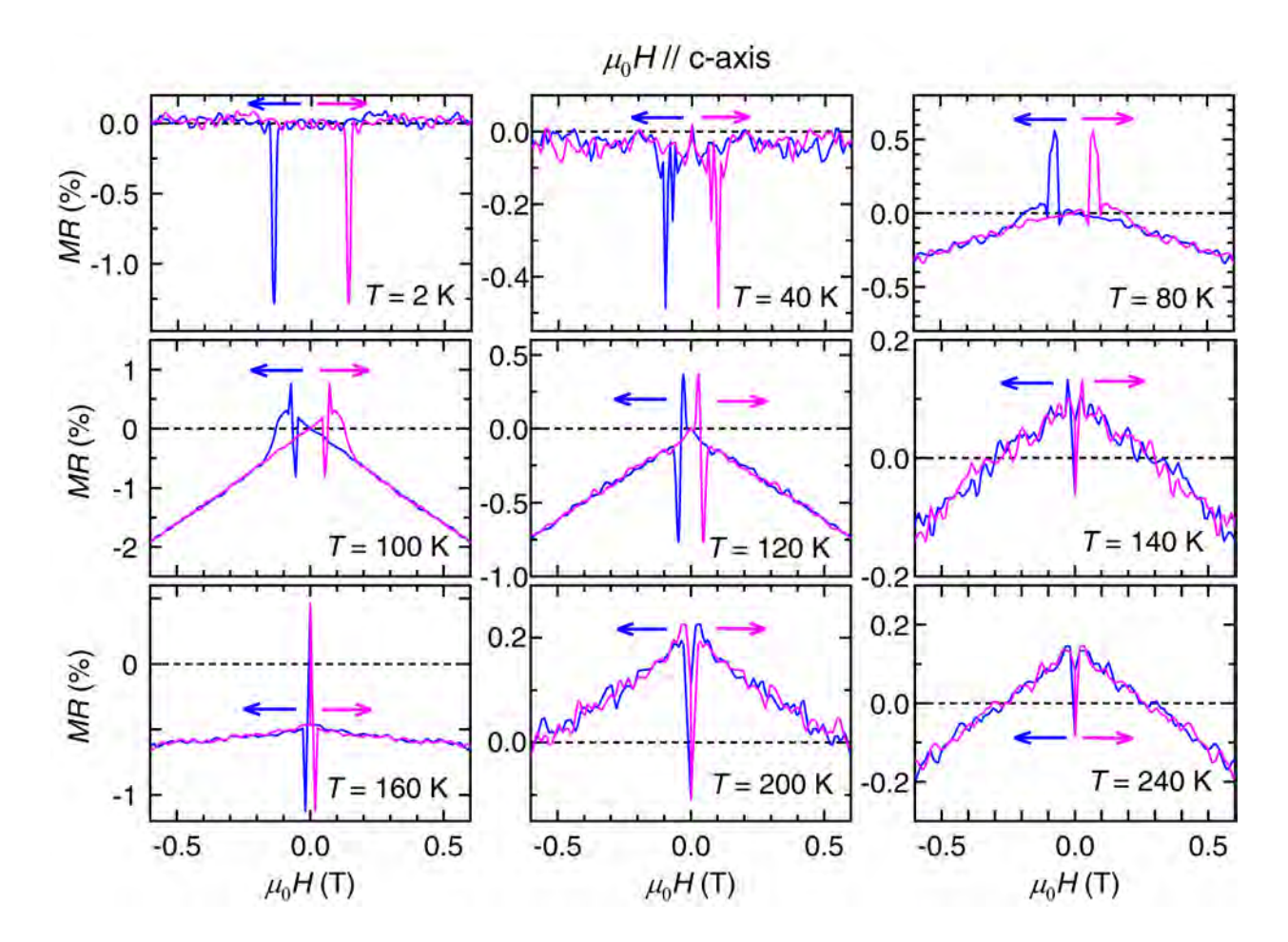


Figure S2. Transverse magnetoresistivity MR as a function of the magnetic field $\mu_0 H$ applied along the c-axis of a 15 nm thick Fe_{5-x}GeTe₂ crystal for several temperatures. Here, $MR = [\rho_{xx}^c(T,\mu_0 H) - \rho_{xx}^c(T,\mu_0 H = 0 \text{ T})/\rho_{xx}^c(T,\mu_0 H = 0 \text{ T})]$. As indicated by horizontal arrows, magenta and blue lines correspond to increasing and decreasing magnetic field sweeps, respectively. Due to the hysteretic behavior of the MR at low fields, for each trace, and after having stabilized the temperature, we took the average value of $\rho_{xx}^c(\mu_0 H = 0 \text{ T})$ prior to sweeping $\mu_0 H$ along each orientation. Notice i) the very small magnetoresistivy, i.e., in the order of a few percent or a fraction of a percent, ii) the decrease in the MR as a function of $\mu_0 H$, implying negative magnetoresistivity due to the field-induced suppression of spin scattering, and iii) the near absence of magnetoresistivity below $T \cong 40 \text{ K}$. Below $T \cong 160 \text{ K}$, sharp and hysteretic peaks, or dips, are observed in the MR. These coincide with the pronounced increase in $\rho_{xy}(T)$ as a function of $\mu_0 H$ prior to its saturation (see, Figures 2 and 3 in the main text). At higher Ts both peaks converge producing dips in the vicinity of $\mu_0 H = 0 \text{ T}$. Most importantly, the hysteresis associated with the position of the peaks and dips in $\rho_{xx}^c(T,\mu_0 H)$ coincide with the values of H_c^c extracted from $\rho_{xy}^c(T,\mu_0 H)$ (see Figure 2 in the main text).

 $Table \ S1|\ Atomic\ coordinates\ of\ Fe_{4.01}Ni_{0.68}GeTe_2\ from\ dingle\ crystal\ X-ray\ diffraction$

Fe_{4.30}Ni_{0.39}GeTe₂ Trigonal, $R\overline{3}m$ (a = 4.037(4) Å, c = 29.11(4) Å)

		X	у	Z	U _{iso} */U _{eq}	Occ. (<1)
Fe1	6 <i>c</i>	0	0	0.0741(3)	0.015(2)	0.296(10)
Ni1	6 <i>c</i>	0	0	0.0741(3)	0.015(2)	0.0502(17)
Fe2	6 <i>c</i>	0	0	0.30925(9)	0.0182(15)	0.855
Ni2	6 <i>c</i>	0	0	0.30925(9)	0.0182(15)	0.145
Fe3	6 <i>c</i>	0	0	0.39669(11)	0.0256(7)	0.855
Ni3	6 <i>c</i>	0	0	0.39669(11)	0.0256(7)	0.145
Ge	6 <i>c</i>	0	0	0.0086(2)	0.019(2)	0.5
Te	6 <i>c</i>	0	0	0.21944(5)	0.0193(4)	

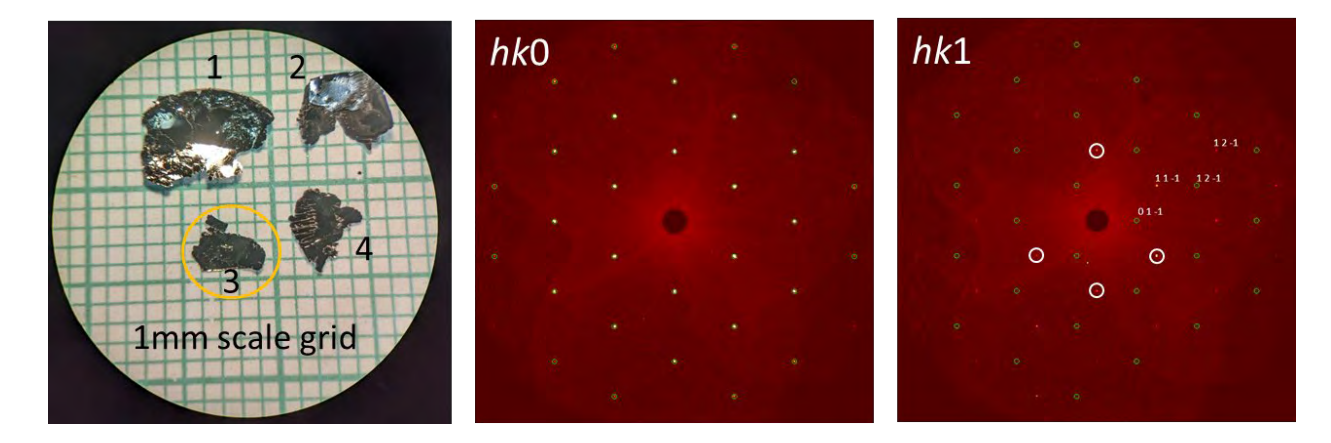


Figure S3. Single crystal X-ray diffraction of Fe_{4.01}Ni_{0.68}GeTe₂. Left panel: picture of a few Ni-doped Fe_{5-x}GeTe₂ single crystals. Center: Precession image of the hk0 plane showing indexed clean bragg reflections used for refinement of the crystal structure. Right: Precession image of the hk1 plane indicating a set of unindexed reflections (select few in white circles) that break reflection condition h+k+l=3n.

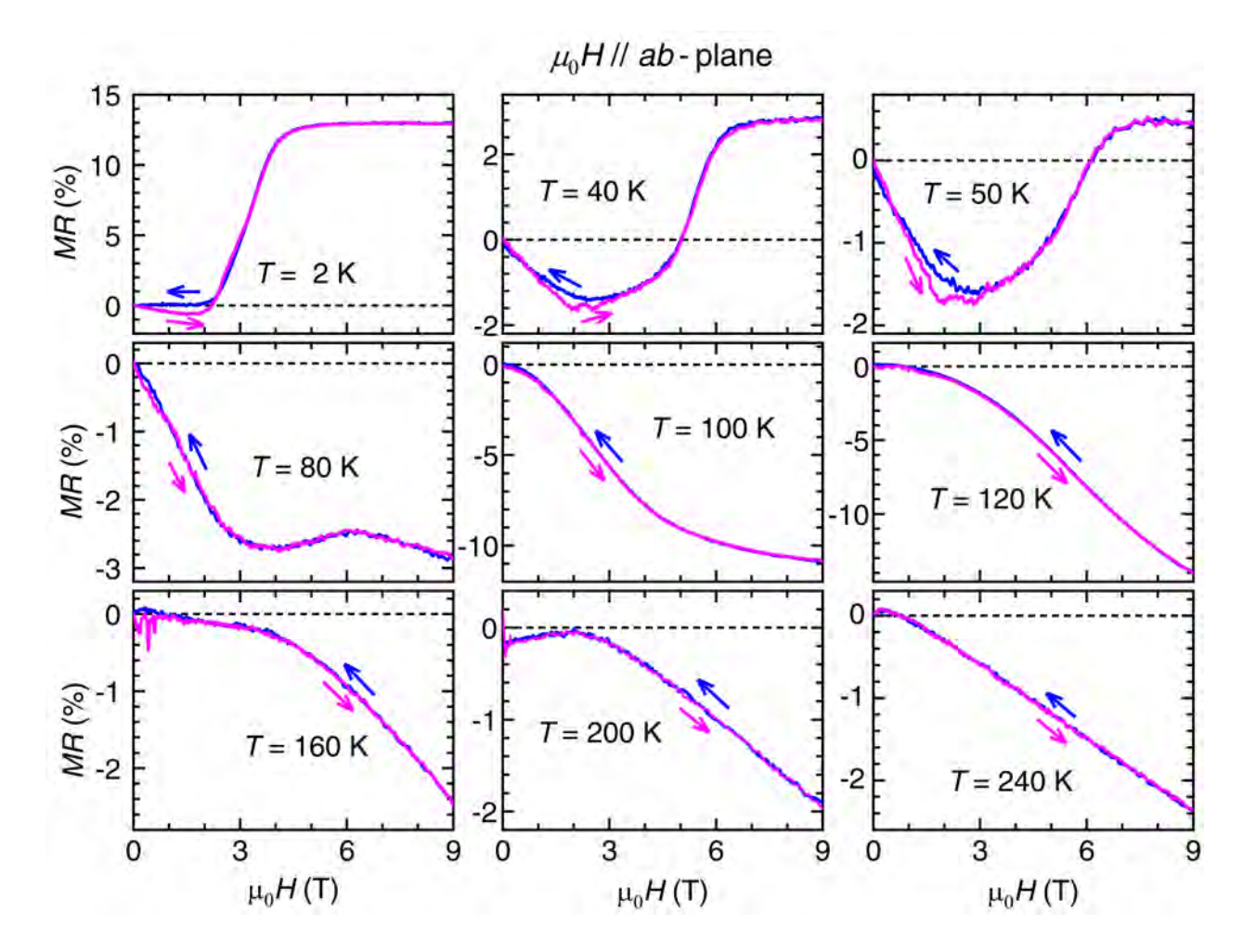


Figure S4. Longitudinal magnetoresistivity MR ($\mu_0H \parallel j$ with j being the current density) as a function of the magnetic field μ_0H applied along the ab-axis for a 15 nm thick Fe_{5-x}GeTe₂ crystal and for several temperatures. Here, $MR = \left[\rho_{xx}^{ab}(T,\mu_0H) - \rho_{xx}^{ab}(T,\mu_0H = 0 \text{ T})/\rho_{xx}^{ab}(T,\mu_0H = 0 \text{ T})\right]$. As indicated by the horizontal arrows, magenta and blue lines correspond to increasing and decreasing magnetic field sweeps, respectively. Due to the hysteretic behavior of the MR at low fields, for each trace, and after having stabilized the temperature, we took the average value of $\rho_{xx}^{ab}(\mu_0H = 0 \text{ T})$ prior to sweeping μ_0H along each orientation. Notice i) how the mostly negative magnetoresistivity becomes positive beyond a certain field value as T is lowered, likely due to a metamagnetic transition towards a spin-polarized state, and ii) the near absence of hysteresis in ρ_{xx}^{ab} for $T \geq 100$ K, which contrasts markedly with the pronounced hysteresis observed in $\rho_{xy}^{ab}(T,\mu_0H)$ (Figure 4 in the main text). This suggests that the hysteresis observed in $\rho_{xy}^{ab}(T,\mu_0H)$ is not completely dominated by the motion and pinning of domain walls, which should also affect the magnetoresistivity. Instead, it suggests that the field-induced reconfiguration of spin textures is likely responsible for $\rho_{xy}^{ab}(T,\mu_0H) \neq 0$ at $\mu_0H = 0$ T, when $T \geq 100$ K.

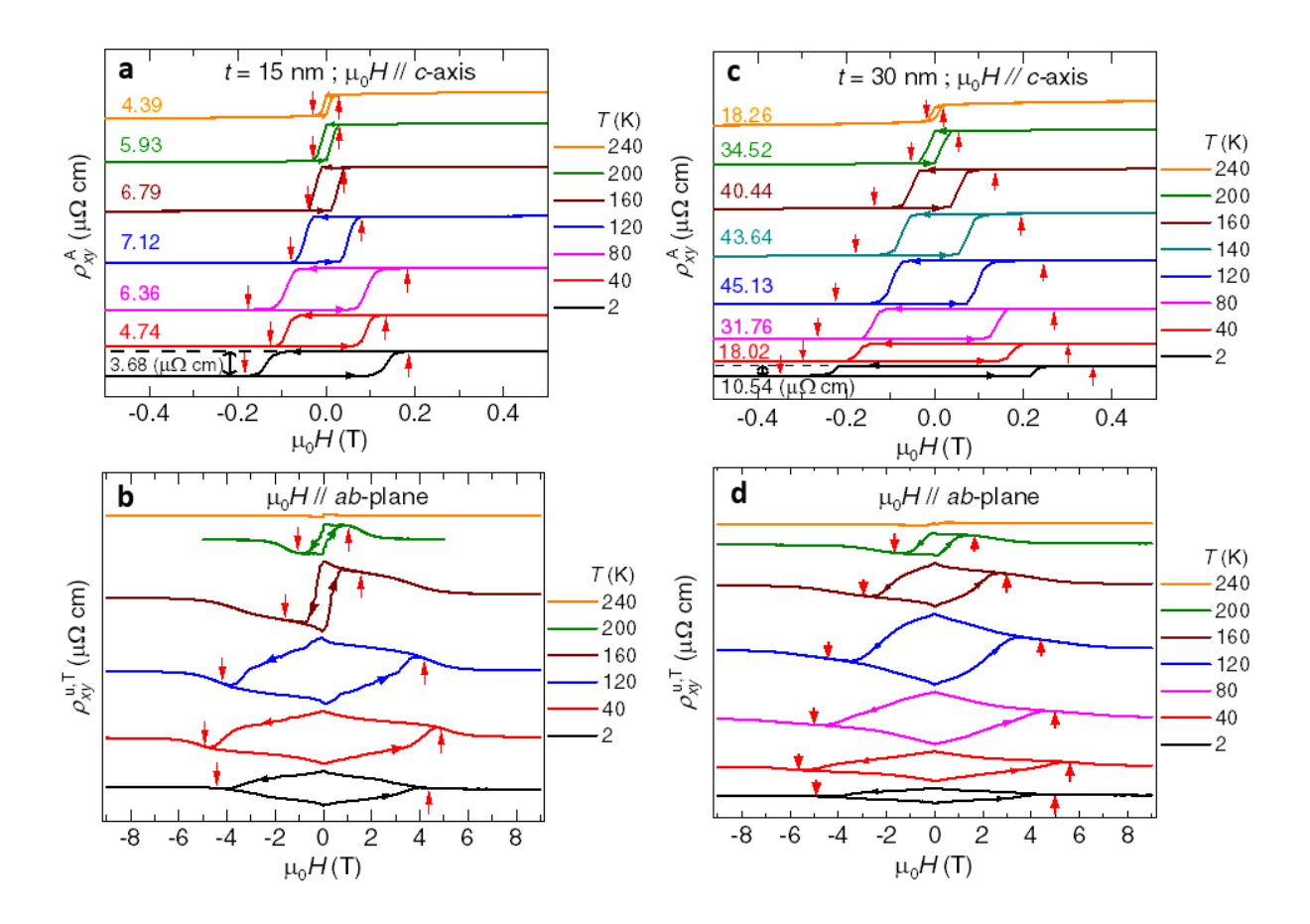


Figure S5. Hysteretic response in both the anomalous Hall and unconventional topological Hall response of exfoliated Fe_{5-x}GeTe₂ crystals. (a) Anomalous Hall resistivity ρ_{xy}^A for a t=15 nm thick exfoliated Fe_{5-x}GeTe₂ crystal as a function of $\mu_0 H$ and for several temperatures. Numbers indicate the absolute change $\Delta \rho_{xy}^A$ as the field is swept from positive to negative values. The maximum $\Delta \rho_{xy}^A$ occurs at temperatures just above the magneto-structural transition. Vertical red arrows indicate the coercive fields H_c^c where the hysteresis loops close. (b) Unconventional topological Hall response $\rho_{xy}^{u,T}$ for the same sample, i.e., for $\mu_0 H \parallel j \parallel ab$ -plane with j being the current density, as a function of $\mu_0 H$ and for several temperatures. Vertical red arrows indicate the coercive fields H_c^{ab} required to close the hysteresis loops. Notice how H_c^{ab} exceeds H_c^c by over one order of magnitude. (c) Same as in a), but for a t=30 nm thick crystal. Notice the increase in both the absolute value of both ρ_{xy}^A and H_c^c . (d) Same as in (b), but for the t=30 nm thick crystal. Notice how the reversible part of $\rho_{xy}^{u,T}$ extends to higher fields. This, and similar data, was used to build Figure 5 within the main text.

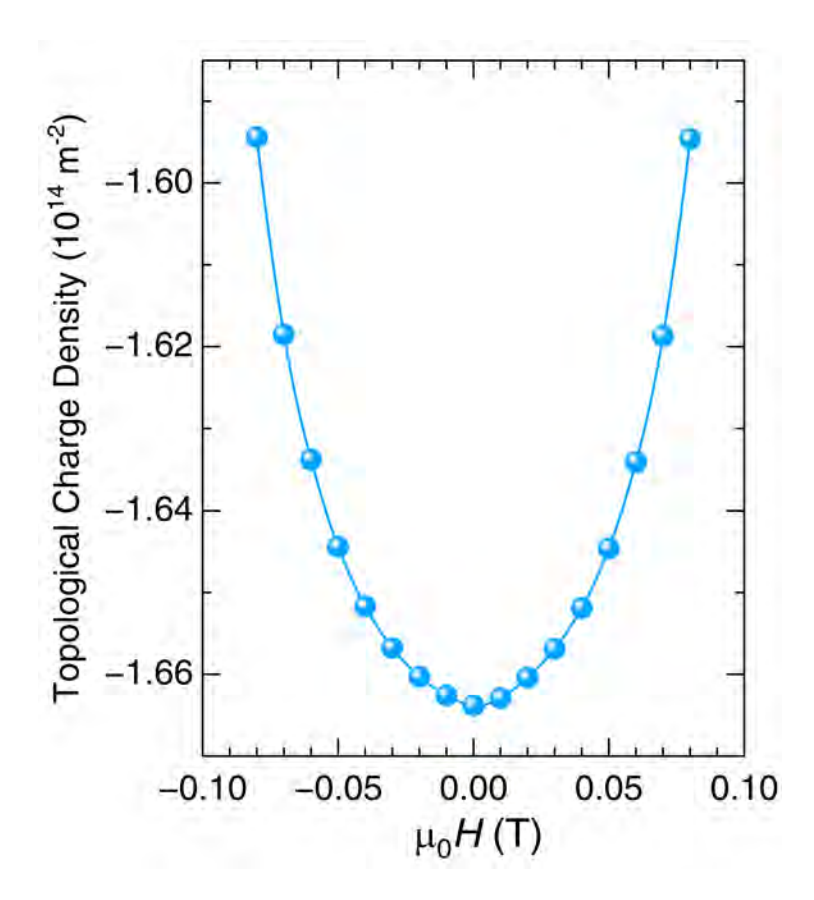


Figure S6. Topological charge density as a function of magnetic field according to micromagnetic simulations. Notice that the absolute value of the topological charge density peaks at zero-field (maximum meron density), precisely where the unconventional topological Hall response displays its maximum value. External magnetic fields applied along an in-plane direction orients the ferromagnetic domains, thus suppressing the topological charges associated to merons.

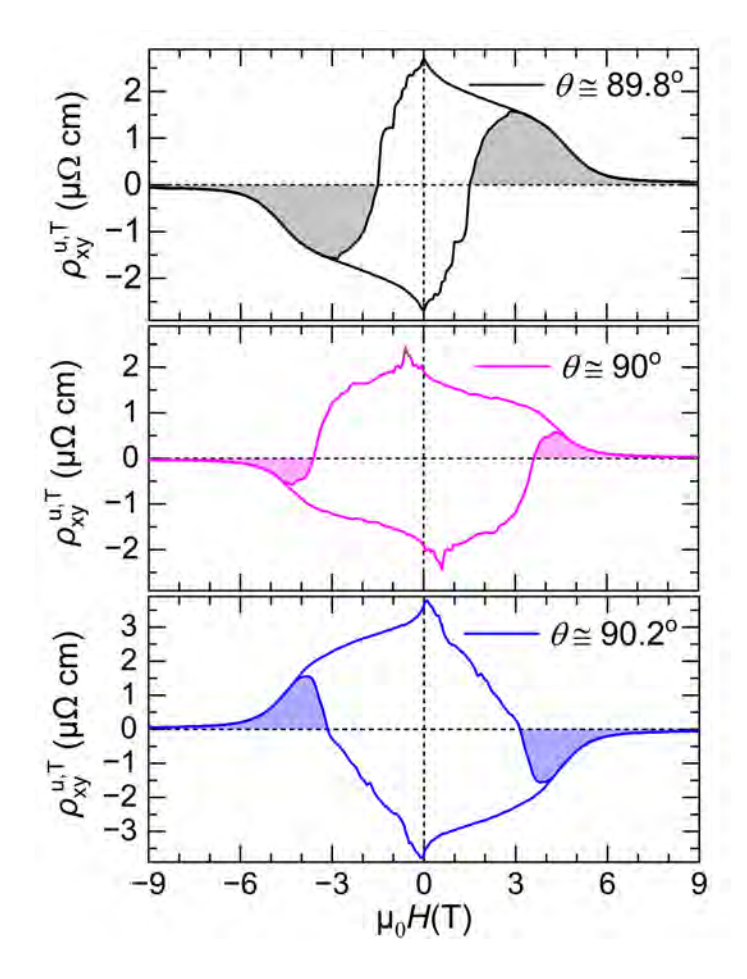


Figure S7. Unconventional topological Hall response for fields very close to the ab-plane. From top to bottom we display $\rho_{xy}^{u,T}(\mu_0 H)$ for a few angles very close to the ab-plane at T=4 K. Notice how the pronounced broad peaks, beyond the irreversible region, change sign indicating that the topological spin textures are written by the out-of-plane component of the magnetic field. Since the $\rho_{xy}^{u,T}(\mu_0 H)$ changes sign, it should reach zero value for fields exactly along a planar direction. However, this precise alignment is very difficult to achieve with conventional mechanical rotators, hence the finite $\rho_{xy}^{u,T}(\mu_0 H)$ response at the nominal value $\theta=90^\circ$.

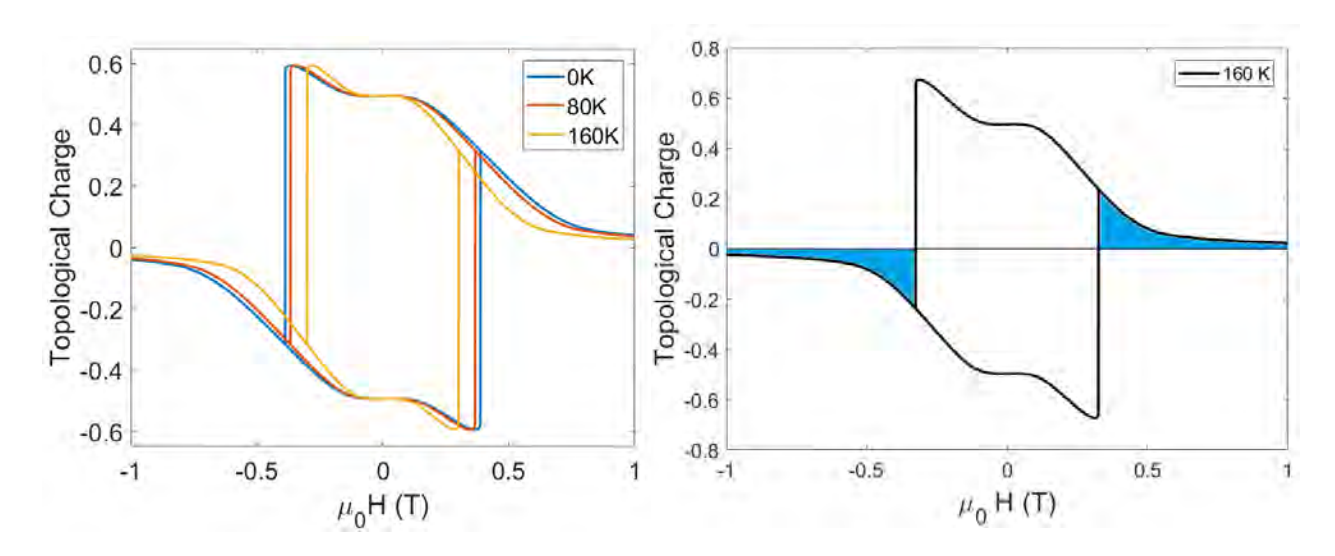


Figure 8: Calculation of the topological charge as a function of inter-planar magnetic field. Left: Topological charge as a function of an out-of-plane field $\mu_0H(T)$ with an absent out-of-plane anisotropy at different temperatures (0 K, 80 K, 160 K), which led to the formation of merons. The width of the loop decreases as function of the temperature as expected, depending on the reduction of the overall magnetization. Right: Similar as Right plot for 160 K with the highlighted areas of finite topological charge.

	M_S	A	K_1	D
0K	$6.3 \times 10^5 \text{ A/m}$	$1.0 \times 10^{-11} \text{ J/m}$	$2.5 \times 10^5 \text{ J/m}^3$	$1.2 \times 10^{-3} \text{ J/m}^2$
80K	$5.97 \times 10^5 \text{ A/m}$	$8.98 \times 10^{-12} \text{ J/m}$	$2.29 \times 10^5 \text{ J/m}^3$	$1.07 \times 10^{-3} \text{ J/m}^2$
160K	$4.88 \times 10^{5} \text{ A/m}$	$6.02 \times 10^{-12} \text{ J/m}$	$1.85 \times 10^4 \text{ J/m}^3$	$7.2 \times 10^{-4} \text{ J/m}^2$

Table S2. Parameters used for the micromagnetic simulations. Thermal parameters used in the simulations for Fig. S8 from Refs.¹⁻³. M_s , A, K_1 , and D are the magnetization saturation, exchange constant, axial anisotropy, and D the Dzyaloshinskii–Moriya interaction constant, respectively.

- (1) Zhang, H.; Chen, R.; Zhai, K.; Chen, X.; Caretta, L.; Huang, X.; Chopdekar, R.V.; Cao, J.; Sun, J.; Yao, J.; Birgeneau, R.; Ramesh, R. Itinerant ferromagnetism in van der Waals Fe_{5-x}Ge Te₂ crystals above room temperature, *Phys. Rev. B* **2020**, *102*, 064417. DOI:10.1103/PhysRevB.102.064417.
- (2) Iturriaga, H.; Martinez, L. M.; Mai, T. T.; Biacchi, A. J.; Augustin, M.; Hight Walker, A. R.; Sanad, M. F.; Sreenivasan, S. T.; Liu, Y.; Santos, E. J. G.; Petrovic C.; Singamaneni, S. R. Magnetic properties of intercalated quasi-2D Fe_{3-x}GeTe₂ van der Waals magnet. *npj 2D Mater. Appl.* **2023**, *7*, 56. DOI: 10.1038/s41699-023-00417-w.
- (3) Casas, B. W.; Li, Y.; Moon, A.; Xin, Y.; McKeever, C.; Macy, J.; Petford-Long, A. K.; Phatak, C. M.; Santos, E. J. G.; Choi, E. S.; Balicas, L. Coexistence of Merons with Skyrmions in the Centrosymmetric van Der Waals Ferromagnet Fe_{5-x}GeTe₂. *Adv. Mater.* **2023**, *35*, 2212087. DOI: 10.1002/adma.202212087.